Title: Nanoscale indentation of plasma membrane establishes a contractile actomyosin scaffold through selective activation of the Amphiphysin-Rho1-Dia/DAAM and Rok pathway

Authors: Tushna Kapoor [ORCID 0000-0001-6003-8535], Pankaj Dubey[a] [ORCID 0000-0001-7532-8332], Seema Shirolikar, and Krishanu Ray [ORCID 0000-0001-6406-3199]*

Department of Biological Sciences, Tata Institute of Fundamental Research, Mumbai 400005, India.

*-Address for correspondence: Krishanu Ray, DBS, TIFR, Mumbai 400005, India. E-mail: krishanu@tifr.res.in, krishanu64@gmail.com, Phone: +91-22-22782730, Fax: +91-22-2280-4610/11.

a- Current address: Blizard Institute, Barts and The London School of Medicine and Dentistry, Queen Mary University of London, 4 Newark Institute, E1 2AT, UK.

Abstract:

Nanoscale bending of plasma membrane increases cell adhesion, induces cell-signalling, triggers F-actin assembly and endocytosis in tissue-cultured cells. The underlying mechanisms are not very well understood. Here, we show that stretching the plasma membrane of somatic cyst cell around rigid spermatid heads generates a stable, tubular endomembrane scaffold supported by contractile actomyosin. The structure resembles an actin-basket covering the bundle of spermatid heads. Genetic analysis suggests that the actomyosin organisation is nucleated exclusively by the Formins, Diaphanous and DAAM, downstream of Rho1, recruited by the Bin-Amphyphysin-Rvs (BAR)-domain protein, Amphiphysin, around the spermatid heads. Actomyosin activity at the actin-basket gathers the spermatid heads into a compact bundle and resists the invasion of the somatic cell by the intruding spermatids. These observations reveal a new response mechanism of nanoscale bending of the plasma membrane, which generates a novel cell adhesion strategy through active clamping.

Keywords: Actomyosin, Amphiphysin, Diaphanous, Rho-1, Rho-kinase, Spermiation, *Drosophila*

Glossary: TE - Terminal epithelium, HCC - Head cyst cell, TCC - Tail cyst cell, NB - Nuclei bundle/Spermatid head bundle, Caplet and Basket - parts of Actin cap, SJs - Septate Junctions, CC-coiled cyst.

29 **Introduction:**

30 The plasma membrane is the ultimate barrier in eukaryotic cells. It also acts as a mechanical force
31 sensor and can withstand severe distortions (Pontes et al., 2013) and indentation up to a few microns
32 by nano-size objects (Yang and Saif, 2007). Nanoscale deformation of the cell membrane increases cell
33 adhesion to the substrate (Viswanathan et al., 2015), and confers cell fate and induces osteogenic
34 differentiation of mesenchymal stem cells (Abagnale et al., 2015). It is also suggested that some
35 viruses are likely to exploit this property to invade the host cell (Wiegand et al., 2020). Therefore,
36 understanding the mechanism of cellular response to plasma membrane indentation is critical to
37 identify the determinant factors.

38 Nanoscale bending of plasma membrane acts as hotspots for clathrin-dependent endocytosis
39 (Zhao et al., 2017), which is likely to signal the cell and provide access to the pathogens. The bending
40 of the plasma membrane due to the tight wrapping of ~100 nm diameter nanopillars is sensed by
41 Clathrin which induces dynamin mediated endocytosis (Zhao et al., 2017). On the other hand, the
42 bending of the basolateral cell membrane around nanopillars of diameters ~100-400 nm triggers local
43 F-actin assembly through the recruitment of Formin-Binding-Protein-17 and Arp2/3 activation (Lou et
44 al., 2019). Thus, molecular response to nano-indentation of the plasma membrane appears to depend
45 on the surface topography. The underlying mechanism is, however, not investigated. Moreover, all
46 these studies are carried out *in vitro* using synthetic conditions. Hence, these conjectures and their
47 biological relevance are yet to be established *in vivo*.

48 In *Drosophila* testis, 64 spermatids mature synchronously within a somatic cell enclosure
49 formed by the head-cyst-cell (HCC) and tail-cyst-cell (TCC) that are held together by septate junction
50 (SJ) proteins (Dubey et al., 2019). Each mature spermatid head is a rigid, ~10 µm long rod of ~200 nm
51 diameter. As the cyst matures, it moves through the terminal epithelium (TE) region at the base of the
52 testis until mature spermatids are released from the cyst enclosure, and progress into the seminal
53 vesicle (SV) (Dubey et al., 2016). During this last stage, spermatid heads push against the plasma
54 membrane of the HCC and an actin-rich structure (actin cap), contributed by the somatic cyst cell,
55 appeared to hold the spermatid heads and prevent premature release by rupturing the HCC (Desai et
56 al., 2009; Dubey et al., 2016). Actin cap is composed of two distinct domains that are clearly separated
57 from each other - a relatively stable actin-rich 'basket' domain envelopes the sperm head bundle,
58 whereas the 'caplets' form around the HCC membrane whenever a sperm head intrudes beyond 2 µm
59 from its resting position (Dubey et al., 2016). Every attempt of a spermatid head intrusion is
60 immediately repulsed by transiently assembled caplets which are formed by the WASp-Arp2/3-
61 dependent process around the indented plasma membrane of the HCC (Dubey et al., 2016). The caplet

62 disappears as soon as the intruding spermatid head reverts to its initial position. The mechanism of
63 the basket assembly, which persists even after the spermatid release, was not explored.

64 Here, we provide a comprehensive sub-cellular and molecular-genetic evaluation of the
65 basket assembly that helped to derive a novel clamping mechanism. We find that the basket is
66 composed of a highly tubular membrane scaffold supported by actomyosin. It is assembled exclusively
67 through concerted activities of the Rho1 GTPase, and the formins Diaphanous (Dia) and DAAM. The
68 Bin-Amphiphysin-Rvs (BAR) domain protein, Amphiphysin (Amph), possibly recruits Rho1 at the
69 basket. Rho1 recruits and activates nonmuscle myosin-II (NM2) through Rho-kinase (Rok). The
70 actomyosin activity maintains the integrity of the actin-basket and holds the spermatid heads together
71 in a parallel bundle, which is essential for maintaining male fertility (Dubey et al., 2019). Basket domain
72 also prevents the penetration of the somatic cell by spermatid heads. Together, these results describe
73 an unprecedented role of membrane bending in triggering the assembly of an actomyosin clamp at
74 the plasma membrane. We postulate that the bending of the HCC plasma membrane around
75 spermatid heads triggers the recruitment of specific BAR-domain proteins to initiate the basket
76 assembly, and discuss the significance of these findings in the context of wound healing and tissue
77 morphogenesis.

78

79 **Results:**

80 **Actin-Basket consists of extensively tubular endomembrane and F-actin**

81 The cysts containing coiled spermatids, with characteristic compacted NBs (Fig 1A; arrows, Fig 1B) are
82 found within the TE zone. During the initial stage of individualisation, F-actin cones (Investment
83 Complex – IC) consisting of dendritic actin form around each spermatid head (arrowhead, Fig 1B; Fig
84 S1A), and move down the tail (Noguchi and Miller, 2003). As the ICs progressed, the spermatid heads
85 were rearranged in a parallel bundle (Nuclei Bundle – NB, Fig S1B-E), and a different type of F-actin
86 structure, called actin cap (Desai et al., 2009), appears inside the HCC around the NB (yellow
87 arrowheads, Fig S1C-E). Actin cap consists of a dense F-actin basket and multiple caplet domains
88 (Dubey et al., 2016) (arrowhead and arrow, Fig S1F). The basket is most pronounced in the middle
89 region of the TE, which had fully coiled spermatid tails (arrowhead, Fig S1F).

90 To get a more comprehensive understanding of the actin cap, which is formed inside the HCC
91 (Desai et al., 2009), we used a combination of confocal and Structured Emission Depletion (STED)
92 microscopy. We used *PpYGal4*, which expresses at a relatively higher level in the HCC during the
93 terminal stage of spermatid differentiation. The *PpY>GFP-utr* expression marked caplets (arrows, Fig

94 1C-C'), as well as a dense F-actin basket, surrounding the NB (arrowheads, Fig 1C-C'). In addition, we
95 noted F-actin sleeves around individual spermatids (open arrows, Fig 1C-C'), henceforth referred to as
96 'actin sleeves'. The actin sleeves present in between each spermatid head in an NB were also
97 prominent in the STED images (open arrows, Fig 1D-D'''). The caudal part of the actin sleeves, marked
98 by Phalloidin, but not by GFP-Utr (dashed open arrow, Fig 1C-C'; open arrows, Fig 1D''-D''') are most
99 likely contributed by the TCC, since mature sperms released into the SV do not stain for F-actin.

100 As described earlier (Tokuyasu et al., 1972b), Transmission Electron Microscopy (TEM) of
101 transverse sections of NBs indicated that individual spermatid heads are tightly wrapped by the HCC
102 membrane (arrows, Fig 1E). The HCC membrane is highly tubulated at the rostral end of the spermatid
103 heads (arrowheads, Fig 1E), which are buried deep into the HCC. The membrane tubules also had
104 bulbous termini (arrowheads, Fig 1F-G), and electron-dense material coated the membrane buds
105 (arrowhead, Fig 1F). These structural features resembled the tubulobulbar-complex found around
106 individual spermatid heads inside Sertoli cells in mammalian testis (Guttman et al., 2004). Such tubules
107 were not detected near the HCC-TCC interface (arrows, Fig 1H), which is held together by SJs (Dubey
108 et al., 2019). Together, these analyses indicated that each spermatid is tightly ensleeved with the
109 somatic cell membrane supported by F-actin (actin sleeve), and the head bundle (NB) is surrounded
110 by a highly tubular actin-rich membrane, which we redefine as the 'basket' domain (Fig 1A") (Video
111 S1).

112 The baskets were classified in two categories - *mature* baskets with distinctively rich Phalloidin
113 staining (Fig 1C; S1F), and relatively *thin* ones with barely detectable Phalloidin staining surrounding
114 the NB (Fig S1G-G'). These two morphological classes were also distinguished by significantly different
115 F-actin volume (Fig S1H). Altogether, these observations indicated that the basket domain forms
116 around the spermatids heads as the coiled spermatids progress into the TE.

117 **Basket domain is a contractile structure composed of relatively stable F-actin**

118 *Ex-vivo* time-lapse imaging of *Drosophila* testes expressing *sqh::utr-GFP* and *ProtB-dsRed,* marking the
119 F-actin and the NB, respectively, revealed that the basket periodically contracts and expands along
120 the axis parallel to the NB (Fig 2A; Video S2). To understand the effect of periodic basket contraction,
121 we used high-intensity pulsed IR laser (800 nm) to ablate a part of the basket. Focussing the laser
122 beam in a 0.75 μm^2 (10x10 pixels) area near the edge of the basket region caused an isotropic
123 retraction of F-actin from the centre of the spot (asterisk, Fig 2B, B"). Over time, the F-actin
124 surrounding the NB dispersed (follow arrowheads, Fig 2B) and accumulated at the caplet region
125 (arrow, 30' 56", Fig 2B; Video S3) with concomitant sheering of the NB (Fig 2B'). To ensure that the
126 loss of F-actin from the basket region caused NB disruptions, we ablated a control spot in the HCC

127 cytoplasm, away from the basket (dashed region, Fig 2C-C') using the same laser power. It did not
128 perturb the caplet and the basket (arrows and arrowheads, Fig 2C), as well as the NB organisation (Fig
129 2C'; Video S4). These results suggested that that basket is a contractile structure required for
130 maintaining the spermatid heads in a tight bundle.

131 Further, the Fluorescence Recovery After Photobleaching (FRAP) revealed that the F-actin at
132 the basket domain is composed of stable and dynamic components (Video S5). The post bleach
133 recovery (t= 5.5'' onwards, Fig 2D-D') reached saturation within 100 seconds (Fig 2E). The data were
134 fitted to a single exponential using the Levenberg-Marquardt iteration algorithm, and the maximum
135 recovery was found to be 0.49 ± 0.006, indicating nearly equal amounts of mobile and immobile
136 fractions of F-actin. Hence, nearly 50% of the F-actin at the basket domain appeared to remain stable
137 for a considerable period.

138 We also noted that thin F-actin-rich extensions (actin tubules) occasionally emanate from the
139 basket domain (open arrowheads, Fig S2; Video S6). These structures may contribute to the partly
140 dynamic nature of the basket, and may potentially mark the tubular membrane extensions observed
141 by the TEM (Fig 1E, G).

142 Together, the anatomical data and the time-lapse analyses suggested that a relatively stable
143 membrane-actin assembly around the spermatid heads during the final stages of spermatid
144 maturation maintains them in a tight bundle. We wanted to understand how such a complex and
145 unprecedented structure forms and its biological relevance.

146

147 **Rho1 activation organises the F-actin assembly at the Basket domain**

148 *Drosophila* genome codes for Rho1 (Rho A in mammals), three different Rac isoforms, and a
149 Cdc42 orthologue (www.flybase.org). To understand the molecular mechanism of F-actin assembly in
150 the basket domain, we knocked down, as well as altered the functions of these three classes of Rho
151 GTPases in the cyst cells, using *PpYGal4*. Three quantitative parameters - the number of intact NBs,
152 progressed ICs and basket morphology - were used to ascertain the cellular and biological impact of
153 these perturbations. Loss of actin cap disrupts the NB and leads to premature release inside the testis
154 (Desai et al., 2009; Dubey et al., 2016). Therefore, we counted the number of intact NBs at the base
155 of the testes to determine the effects of the tissue-specific perturbations (arrows, Fig 3A). Loss of F-
156 actin assembly during the individualisation stage, preceding the spermatid coiling, affects the IC
157 assembly and progression, and the NB packing (Ghosh-Roy et al., 2005). Therefore, we estimated the
158 number of progressed ICs, to determine whether the effect was restricted to the final stage of sperm

159 maturation. Third, we analysed the basket morphology and volume marked by the Phalloidin staining,
160 as well as the anisotropy of NB packing to understand the effects at the subcellular level.

161 The *PpY>Rho1 RNAi* combination was lethal. Knockdown of Rho1 using the relatively milder
162 *SG18.1Gal4,* survived to the adult stage. The TE region contained mostly disrupted NBs (yellow dashed
163 circle, Fig 3B-B', F) and very few progressed IC (Fig 3G; arrowheads, Fig S3B). The overexpression of
164 dominant-negative Rho1-N19 using *PpYGal4* reduced the number of intact NBs (Fig 3C-C', F) without
165 affecting the progressed ICs (Fig 3G; arrowheads, Fig S3C). A higher proportion of these NBs was
166 associated with visibly thin or deformed baskets (open arrows, Fig 3I-I'; pie chart), as compared to
167 control (Fig 3H-H'; pie chart). The expression of constitutively-active Rho1-V14 (*PpY>Rho1CA*)
168 increased the number of NBs (Fig 3D-D', F) and the proportion of mature baskets (Fig 3J-J'; pie chart),
169 without altering the number of progressed ICs (Fig 3G; arrowheads, S3D). Rho1 overexpression also
170 significantly increased the fraction of NBs associated with mature baskets (pie chart, Fig 3K), although
171 there were no changes to the total number of NB (Fig 3E-E', F) and progressed ICs (Fig 3G; arrowheads,
172 Fig S3E). Thus, Rho1 activity is implicated in the F-actin assembly at the basket domain. Finally, Rho1
173 immunostaining revealed a visible enrichment only at the basket domain, and not at the caplets
174 (arrowhead and arrow, Fig 3L-L'). Together these results indicated that Rho1 localisation and
175 activation at the basket domain are essential for the F-actin assembly.

176 Next, we tested the roles of Cdc42 and Rac1. The *PpY>Cdc42 RNAi* testes were shrunken, with
177 no identifiable mature cysts (Fig S4C-D), suggesting that Cdc42 has a broader role in sperm
178 differentiation. Overexpression of the dominant-negative *Cdc42-L89* significantly increased the
179 average number of intact NBs (Fig S4E, P), but there were no identifiable defects in the basket
180 morphology (Fig S4F-F'). Hence, we ruled out a direct involvement of Cdc42 in the basket assembly.
181 The *Rac1* and *Rac2 RNAi*, as well as the overexpression of the dominant-negative Rac1-N17 and Rac1-
182 L89, respectively, did not change the NB and IC counts (Fig S2). However, we noticed an unusually
183 large number of actin tubules emanating from the basket in the *Rac1 RNAi* and DN backgrounds
184 (yellow arrowheads, Fig S2H-H', L-L'). Also, the Rac1-GFP, expressed from its endogenous promoter,
185 was moderately enriched in and around the basket (arrowhead, Fig S4O-O'). Thus, we concluded that
186 Rac1 is likely to maintain actin tubule dynamics. Together, these results suggested that though Rac1
187 is not directly involved in the basket assembly, it may fine-tune actin-membrane dynamics in the
188 basket.

189 In summary, tissue-specific perturbation of different class of Rho-GTPases in the cyst cells
190 suggested that the basket domain is exclusively formed due to the activation and recruitment of Rho1.

191 These observations also raised two specific questions – whether the recruitment and activation of
192 Rho1 lead to the F-actin assembly at the basket domain and how Rho1 is recruited.

193

194 **Basket is composed of linear F-actin nucleated by the formins - Diaphanous and DAAM**

195 The association of GTP-bound Rho1 activates a sub-group of the formin class of the F-actin nucleation
196 promotion factors (Kuhn and Geyer, 2014). Therefore, to identify the role of formins in the basket
197 assembly, we separately expressed RNAi constructs for all the six formins coded by *Drosophila* genome
198 (Breitsprecher and Goode, 2013), *viz.*, Diaphanous (Dia), Dishevelled Associated Activator of
199 Morphogenesis (DAAM), Formin-like (Frl), Formin 3 (Form 3), Formin homology-2 domain-containing
200 (Fhos) and Cappuccino (Capu), using *PpYGal4*. The *dia RNAi* expression led to a severe loss of coiled
201 NBs (Fig 4B-B', D) with no significant change in the number of progressed ICs (Fig 4E; S5B). We also
202 noticed a large number of free spermatid heads in the TE in *dia RNAi* testes (yellow dashed circle, Fig
203 4B-B'), suggesting that NBs were disrupted after individualisation. Amongst the few remaining intact
204 NBs, more than 35% ($p = 0.0086$) were associated with severely deformed and thin baskets (Fig 4G-
205 G'; pie chart) with significantly lower volume (Fig 4I). Furthermore, the NB anisotropy estimate
206 revealed a lower trend (i.e., less ordered arrangement), although the difference was not statistically
207 significant (Fig 4J). The *DAAM RNAi* also caused a significant, but comparatively smaller reduction of
208 NBs (Fig 4C-D) than *dia RNAi*, with no alteration in the number of progressed ICs (Fig 4E, S5C). Similar
209 to the *dia RNAi*, nearly one-third of the baskets in the *DAAM RNAi* testes were thin and deformed (Fig
210 4H-H'; pie chart) with marginally decreased volume (Fig 4I), suggesting that DAAM may also be
211 involved in the basket assembly. However, we did not observe a change in NB anisotropy (Fig 4J).
212 Together, these observations implicated both Dia and DAAM in the basket assembly.

213 Although Frl and Form3 RNAis also severely reduced the number of intact NBs (Fig 4D; S5D,
214 G), the number of progressed ICs were also reduced significantly (Fig 4E; S5F, I). A few remaining NBs
215 that we found in these backgrounds appeared to have intact baskets (arrowheads, Fig S5E, H), but we
216 could not quantify their morphology, as the number of intact NBs was insufficient. Hence, we
217 concluded that the NBs were lost due to considerable disruption of an earlier differentiation process.
218 Lastly, the expression of Fhos and Capu RNAis did not affect NB (Fig 4D; S5J, M) and IC (Fig 4E; S5 L, O)
219 counts. The basket morphologies were also similar to that of control (Fig S5 K, N, P). Also, the Capu-
220 GFP did not localise at the basket (Fig S5Q-Q'). Therefore, the role of Fhos and Capu in basket assembly
221 was ruled out. Overall, on the basis of the genetic perturbations, the roles of formins in spermatid
222 maturation can be categorised as- affecting NBs but not ICs (Dia and DAAM), affecting both NBs and
223 ICs (Frl and Form 3), and affecting neither NBs nor ICs (Fhos and Capu).

224 Altogether, the genetic analysis suggested that the basket is exclusively formed through Dia
225 and DAAM. Consistent with this conjecture, we found a visible enrichment of Dia at the basket region
226 (arrowhead, Fig 4K-K'). Together, the results suggested that the basket is contractile actin structure
227 formed by Rho1, Dia and DAAM activities.

228

229 **F-BAR protein, Amphiphysin, recruits Rho1 and activates the F-actin assembly at the basket domain**

230 Local tension and curvature of the membrane bilayer trigger F-actin assembly (Aspenstrom, 2014;
231 Yang and Saif, 2007). TEM sections revealed that extensively folded membrane surrounds the
232 spermatid heads (Fig 1E-G), and time-lapse observations after the laser ablation (Fig 2B) suggested
233 that the spermatid heads continuously press onto the HCC. Hence, mechanical tension along the HCC
234 plasma membrane could initiate the F-actin assembly forming the basket domain. Association of the
235 Clathrin-family of coat protein complex also bends and stabilises the membrane curvature, and
236 promotes endocytosis (Hinrichsen et al., 2006). Also, the association of BAR-domain proteins with
237 negatively-charged membrane stabilises the membrane curvature and activates the BAR-proteins,
238 which sequester specific Rho-GTPases (Aspenstrom, 2014).

239 Expression of the GFP-tagged Clathrin-light-chain (*PpY>eGFP-Clc*, Fig 5A) and the BAR-domain
240 protein Syndapin (*PpY>Synd-GFP,* Fig 5B-B') in the HCC marked the actin cap. The eGFP-Clc expression
241 surrounded the basket and the caplet domain (arrowhead and arrow, Fig 5A-A'), whereas Synd-GFP
242 co-localised with the F-actin of the basket domain (arrows, Fig 5B-B'). Synd associates with the curved
243 membrane through the SH3 and the BAR-domain. The negatively charged Phosphatidylinositol 4, 5-
244 bisphosphate (PIP_2) is essential for Syndapin binding (Takeda et al., 2013). Overexpression of Synd-
245 SH3-eYFP (Fig S6A-A') marked the basket, whereas that of the Synd-R129E R130E-eYFP, carrying
246 mutations in the PIP_2 interacting residues of the BAR domain, failed to mark the basket (Fig S6B-B').
247 This result further indicated that the basket domain is rich in the negatively charged membrane,
248 particularly PIP_2. Therefore, to understand the role of membrane remodelling proteins in this process,
249 we performed a limited RNAi screen.

250 Clathrin consists of three heavy chains, each associated with a light chain. This triskelion
251 arrangement forms a cage-like lattice on the membrane (Kirchhausen et al., 2014). The clathrin heavy
252 chain (chc) and light chain (clc) RNAis did not alter the number of intact NBs in the TE (Fig 5E; S6E, G),
253 as well as the progressed ICs (Fig 5F; S6F, H). However, we noticed a small but significant decrease in
254 the number of mature baskets in the *chc RNAi* background (p=0.040, pie chart, Fig 5H). A similar
255 reduction was seen in *clc RNAi* testes, but the difference was not significant (pie chart, Fig 5I). Hence,

256 we concluded that though Clathrin may control the membrane flux in the basket region, it is unlikely
257 to have a central role in the basket assembly.

258 Amongst the BAR-domain proteins, Synd (de Kreuk et al., 2011), Amphiphysin (Amph)
259 (Yamada et al., 2009), Cdc42 interacting protein (Cip4) (Fricke et al., 2009), Insulin Receptor Substrate
260 53 kDa (IRSp53) (Goh et al., 2012) and Protein Interacting with C Kinase 1 (PICK1) (Rocca et al., 2008)
261 are implicated in actin polymerisation. Synd/PASCIN overexpression recruited Dia at the
262 pseudocleavage furrows of *Drosophila* embryos (Sherlekar and Rikhy, 2016), the Cip4 binding
263 antagonised Dia-induced actin polymerisation (Yan et al., 2013), and IRSp53 binds to mDia during
264 filopodia extension (Goh et al., 2012). PICK1, on the other hand, is indicated to inhibit Arp2/3 (Rocca
265 et al., 2008) and recruit F-actin to the site of endocytosis through myosin (Madasu et al., 2015) in
266 different contexts. Since Dia, and potentially DAAM, are required for basket actin polymerisation, we
267 tested the role of all these BAR-domain proteins in the basket assembly.

268 The *Synd*, *IRSp53* and *PICK1 RNAis* did not affect the number of intact NBs (Fig 5E; Fig S6I, N,
269 Q) and the IC progression (Fig 5F; Fig S6J, O, R). The basket morphology of *synd RNAi* testes was also
270 not significantly different from that of the control (Fig 5J-J'; pie chart). Similar results were obtained
271 due to the overexpression of the dominant-negative Synd-R129E R130E-eYFP (Fig S6C-D). Together,
272 these data ruled out a role of Synd/PASCIN, IRSp53 and PICK1 in the basket assembly.

273 In *amph RNAi* testes, there was a significant reduction in intact NBs (Fig 5E, K-K') with a large
274 proportion of them having relatively thin baskets or only actin sleeves (open arrow and pie chart, Fig
275 5K-K'). The IC progression was not affected (Fig 5F; Fig S6K). The defect was even more severe in the
276 *Cip4 RNAi* testes (Fig 5E, L-L'; Fig S6L). However, Cip4 RNAi also significantly reduced the number of
277 progressed ICs (Fig 5F; Fig S6M), suggesting that the loss of NB could be contributed by the disruption
278 of the upstream differentiation process.

279 Finally, the Rho1 enrichment surrounding the NBs associated with the thin baskets was
280 eliminated in *amph RNAi* background (Fig 5N-N'). This observation is consistent with a recent study
281 which suggested that Rvs 167, the budding yeast homologue of Amph, is essential for the localisation
282 of Rho1, in both a Rho GEF dependent and independent manner during cytokinesis (Cundell and Price,
283 2014). Rho1 accumulates at the cytokinetic furrow in a PIP_2-dependent manner (Yoshida et al., 2009).
284 Furthermore, the association of the BAR domain proteins stabilises phosphoinositide domains (Zhao
285 et al., 2013). Hence, we concluded that Amph and possibly the PIP_2 recruitment and stabilisation on
286 the HCC membrane surrounding the spermatid heads could recruit and activate Rho1, and promote
287 the F-actin assembly, as well as the basket morphogenesis.

288 **Non-muscle myosin-II maintains the F-actin structure and the integrity of the basket domain**

289 Time-lapse imaging revealed that the basket is a contractile structure (Fig 2A). In addition to Formins,
290 the GTP-bound Rho activates a serine/threonine kinase called the Rho kinase (Rok/ROCK), which
291 regulates several cytoskeletal rearrangements by phosphorylating a large number of target proteins
292 (Amano et al., 2010). The Rok-GFP expression under the regulatory myosin-light-chain (*spaghetti-*
293 *squash*) promoter (*sqh::Rok-GFP*) highlighted Rok enrichment in the basket domain (arrowhead, Fig
294 6A-A'). One of the downstream targets of Rok is Spaghetti-squash (Sqh), the *Drosophila* orthologue of
295 the regulatory light chain (RLC) of the non-muscle-myosin-II (NM2) (www.flybase.org). NM2 exists in
296 an auto-inhibited folded confirmation. The phosphorylation at Thr 20 and/or Ser 21 of Sqh/RLC
297 relieves the heavy-chain (HC) (Zipper/ Zip in *Drosophila*) auto-inhibition and leads to oligomerisation
298 of NM2 into bipolar filaments. Active NM2 oligomers crosslink F-actin into antiparallel bundles and
299 generate contractile force along the filament (Liu et al., 2017). NM2 drives morphogenetic
300 movements, such as dorsal closure, cytokinesis, and wound healing (Franke et al., 2010). We found
301 that both Zip/HC and Sqh/RLC localise at the basket in the *PpY>zip-GFP* (Fig 6B-B') and *sqh::sqh-GFP*
302 (Fig 6C-C') backgrounds. Also, phosphorylated Sqh/RLC (p-MLC) immunostaining exclusively labelled
303 the basket domain (Fig 6D-D'). Thus, Rho1-dependent recruitment and activation of Rok are likely to
304 promote the NM2 association with the basket.

305 In addition to the contractile behaviour, the laser ablation study suggested that basket
306 maintains the spermatid heads in a tight bundle (Fig 2B). Therefore, to understand whether an
307 actomyosin contraction is responsible for bundling the spermatid heads together, we perturbed the
308 functions of the Rok and NM2 complex in cyst cells. Expression of the *Rok RNAi* (Fig 6F-F') and the
309 dominant-negative *YFP-zip DN* transgene, lacking the actin-binding motor domain (Fig 6H-H') by *PpY-*
310 *Gal4* caused abnormal accumulation of disrupted spermatid bundles in the TE. These perturbations
311 also reduced the average NBs significantly (Fig 6I) without affecting the progressed ICs (Fig 6J; S7A, C).
312 Also, *sqh* knockdown (*Mlc RNAi*) severely affected both NB integrity and IC progression (Fig 6I-J; S7D-
313 E). As expected, the overexpression of the constitutive-active Rok catalytic domain (*Rok-CAT*)
314 selectively increased the NB accumulation (Fig 6I), without affecting ICs (Fig 6J; S7B). We also noted
315 that YFP-zip DN failed to localise at the basket domain (magenta, Fig 6N). Altogether, these results
316 indicated that NM2 localises to the basket directly through its motor domain, and the actomyosin
317 activity is essential for either the basket assembly or maintenance or both.

318 In the *Rok RNAi* testes, more than 45% of the NBs were associated with thin or deformed
319 baskets (pie chart, Fig 6L). The average volume of the basket domain was significantly reduced (Fig
320 6O). In contrast, more than 90% of the NBs in the *Rok-CAT* overexpression background had mature

321 baskets (pie chart, Fig 6M), with very similar volume to the control (Fig 6O). The similarity of the results
322 obtained from the Rho1CA (Fig 3) and Rok-CAT overexpression backgrounds suggest that upregulation
323 of the Rho-Rok pathway may stabilise the basket through the NM2 activation, which would reduce
324 the frequency of sperm release causing accumulation of NBs at the testicular base.

325 In both *Rok RNAi* and *YFP-zip DN* expressing testes, the proportion of mature baskets (Fig 6L,
326 N), the basket volume (Fig 6O), and the anisotropy of NB alignment (Fig 6P) were reduced. These
327 results suggested that the NM2 activity is essential for maintaining the F-actin level and the function
328 of the basket required for gathering the spermatid heads.

329 Regulation of the myosin activity is vital to prevent over-constriction of the actomyosin
330 cytoskeleton. The activity of myosin is maintained by reversible phosphorylation of Sqh/RLC through
331 the regulatory Myosin-binding-subunit (Mbs) protein (Mizuno et al., 2002) and the phosphatase -
332 Flapwing (Flw) (Kirchner et al., 2007). Mbs is inactivated through phosphorylation by Rok, which
333 inhibits the dephosphorylation of Sqh/RLC by Flw. Expression of the constitutively-active Mbs-N300,
334 lacking the N-terminal Rok phosphorylation site, reduced the number of intact NBs significantly
335 without affecting the IC progression (Fig 6I-J; S7F, G) which is consistent with the above conclusion.
336 However, contrary to our expectations, *Mbs* and *flw RNAis* had minimal effect on the NB accumulation
337 (Fig S8A), basket volume (Fig S8C) and basket morphology (Fig S8D, E). These results indicate that Mbs
338 and Flw are unlikely to regulate the NM2/RLC function at the basket. Also, the overexpression of
339 catalytically inactive Rok (Rok CAT-KG), the constitutively-active Sqh-EE and the dominant-negative
340 Sqh-AA, lacking both the phosphorylation sites, had no significant impact on NB count and basket
341 volume (Fig S8B and C). We reasoned that the level of Sqh-AA and Sqh-EE expression were inadequate
342 for interfering with the NM2 function at the basket.

343 Together, these results suggested that Rok-mediated activation of NM2 is essential for
344 maintaining the basket domain, and the actomyosin contractility keeps the NB together. Further, we
345 hypothesised that the NM2 activity would also be essential for maintaining the actin-membrane
346 scaffold in the basket region.

347

348 **Rok dynamically maintains the NM2 localisation and F-actin organisation in the basket domain**

349 To test these conjectures, we inhibited Rok activity by treating testis expressing either Sqh-GFP or Utr-
350 GFP with Rockout™, an ATP competitive inhibitor of Rok (Yarrow et al., 2005). Treatment with 200
351 µM Rockout for one hour significantly reduced the number of intact NBs (Fig 7A-C) and accumulated
352 disrupted spermatids within the TE (yellow dashed circle, Fig 7B). Although the DMSO treatment also

353 caused some abnormality, (arrowheads, Fig 7A-A'), the defects were severely enhanced upon Rockout
354 treatment (Fig 7B-B'). It also significantly disrupted the basket morphology (Fig 7D, E). Depth coding
355 indicated that NBs and associated actin caps remain within a compact volume inside the HCC in control
356 (Fig 7D'-D"). In contrast, most of the NBs appeared disrupted and spread over a large volume after the
357 Rockout treatment (Fig 7E', E''). The treatment also eliminated Sqh-GFP enrichment from the basket
358 (Fig 7D''', E''', and F)

359 The time-lapse imaging further suggested that the Rockout treatment dispersed the Sqh-GFP
360 enrichment around the NB in 30 minutes, and concomitantly the spermatid heads were dissociated
361 from each other (Fig 7H; Video S8), which was not seen upon the DMSO treatment (Fig 7G and I; Video
362 S7 and S9). The treatment also disrupted the basket marked by Utr-GFP in 20 minutes (arrowhead, Fig
363 7J; Video S10). Together these observations suggested that the Rok-dependent NM2 activation
364 localises the myosin motor onto the basket, which maintains the basket integrity and applies a
365 compacting force on the spermatid heads, to keep them in a parallel bundle. However, the Utr-GFP
366 did not disperse from the basket region upon the Rockout treatment. Hence, we concluded that Rok
367 and NM2 are not essential for the F-actin assembly at the basket.

368 Altogether, the above results suggest that mechanical tension on the somatic cyst cell
369 membrane and membrane curvature induced by the intruding spermatid heads could recruit and
370 activate specific BAR-domain proteins, Amphiphysin and perhaps Cip4. The recruitment of BAR
371 domain proteins could further recruit and activate Rho1, triggering the F-actin assembly through the
372 formins, Dia and DAAM. Rho1 also recruits Rok, which activates NM2. Active NM2 crosslinks the actin
373 filaments at the membrane and exerts a lateral clamp-like contractile force gathering the spermatid
374 heads into a tight parallel bundle (Fig 8). The membrane-actomyosin scaffold also resists further
375 intrusion by the spermatid heads.

376

377 **Discussion:**

378 Membrane indentation is the first step of inducing mechanical damage to the plasma
379 membrane. Artificial deformation or indentation of tissue-cultured cells induces actin accumulation
380 at the site of indentation (Lou et al., 2019; Yang and Saif, 2007). Hence, this observation provides the
381 first insight into the events initiated at the start of membrane puncturing *in vivo*. Also, preliminary
382 assessment suggested that the membrane-associated with the basket domain is rich in $PI(4,5)P_2$,
383 which is essential for the interaction with the BAR domain. Therefore, the spermatid head intrusion is
384 also likely to trigger local alteration of lipid metabolism at the HCC plasma membrane. The mechanism

385 that initiates the recruitment of specific BAR-domain proteins to the membrane is unclear. These
386 results suggest that the basket domain would be a useful paradigm to investigate how the membrane
387 tension could alter membrane composition and promote specific recruitment of the N-BAR proteins,
388 particularly the Amphiphysin and potentially Cip4, at the HCC plasma membrane.

389 The BAR-proteins are shown to interact with the Cdc42 and Rac1 family of Rho-GTPases and
390 nucleate F-actin assembly through the WASP/WAVE NPFs (Fricke et al., 2009). A Cip4-like protein,
391 Cdc15/FBP17, is also shown to associate with Dia and DAAM, during the filopodia assembly
392 (Aspenstrom et al., 2006). The consequence of the interaction is still unclear. A separate study further
393 suggested that Cip4 antagonises Dia during the extension of membrane furrows in *Drosophila*
394 embryos (Yan et al., 2013). The genetic analysis suggests that the F-BAR proteins, Amphiphysin and
395 potentially Cip4, could initiate the F-actin assembly at the basket domain in the HCC, exclusively
396 through a Rho-Dia/DAAM-mediated process. The loss of Amph eliminated Rho1 recruitment at the
397 basket domain, as well as F-actin assembly. Thus, the results provide an indication of Amphiphysin-
398 mediated F-actin assembly through Dia and DAAM *in vivo*. Further studies would be required to
399 confirm and understand the molecular basis of this interaction.

400 Above results, together with the earlier report (Dubey et al., 2016), also depict that the HCC
401 membrane curved around each invading spermatid head nucleates two distinct actin networks. The
402 dendritic F-actin associated with caplets form due to WASp-Arp2/3 recruitment and activation in
403 response to the inadvertent invasions, or spermatid head-butting, and is a somewhat transient event.
404 It exerts a counterforce along the direction of invasion to repel every intrusion (Dubey et al., 2016).
405 The F-actin at the basket, nucleated by the Rho1-Dia/DAAM pathway, downstream to Amphiphysin,
406 is relatively stable and applies a lateral contractile force due to actomyosin activity to bundle the
407 spermatid heads together, like a clamp. The genetic and pharmacological analyses show that these
408 two actin networks form independently on two mutually exclusive and radially segregated membrane
409 domains. They also form at different time scales. The caplets are transient and form within minutes
410 of the invasion. Hence, they indicate a cellular response to rapid change in membrane tension. The
411 baskets, on the other hand, grows slowly after individualisation and matures after coiling.

412 The context of the basket assembly provides a clue to the underlying trigger. The HCC and TCC
413 are equally extended during the individualisation stage with their respective plasma membranes
414 tightly stretched around the individual spermatids (Tokuyasu et al., 1972a). Post individualisation, the
415 cysts proceed for coiling, and the HCC contracts (Dubey et al., 2019; Tokuyasu et al., 1972b), which
416 could loosen and fold the excess membrane around spermatid heads triggering the recruitment of
417 Amphiphysin (Fig 8). Therefore, the basket connotes to a response generated due to a change of

membrane tension over time. We also find that the functions of Rho1 and Rac1 are mutually antagonistic at the basket domain, and Rac1 may also have a negative influence on the caplet and tubule dynamics. Thus, the paradigm provides an opportunity to tease out how cells sense, discriminate and respond to stress dynamics in the membrane.

A similar organisation of distinct F-actin nucleation was reported at the immunological synapse in T-cells, and during wound healing in *Drosophila*. At the immunological synapse, three types of actin networks - branched, linear and focal clusters - are arranged in a concentric manner (Hammer et al., 2019). Each of these structures presumably helps in the clustering of proteins such as T-cell receptors. As a result, disruption of the network leads to defects in receptor clustering (Murugesan et al., 2016). Similarly, during the wound closure in *Drosophila* embryo, F-actin networks formed by the Rho1, Rac1, Cdc42 GTPases surround the wound site (Abreu-Blanco et al., 2014). Although Annexin and prepatterning of RhoGEFs were implicated in the Rho GTPases recruitment (Nakamura et al., 2017), how three distinct Rho-GTPase domains assemble on the membrane is still uncertain. Also, since each of these actin networks is partially overlapping, and concentrically arranged, any perturbation to any one of them, affects the others (Abreu-Blanco et al., 2014). Hence, it is challenging to dissect specific roles and mechanisms of regulations.

In comparison, the actin domains on the HCC membrane encompassing the actin cap region are mutually exclusive and well separated. Two distinct mechanical actions trigger them, and we now demonstrated that one could independently perturb the basket and caplets. Therefore, it would be interesting to study how two different F-actin nucleation mechanisms are established on the HCC plasma membrane in real-time during sperm coiling and release in the future.

Finally, a majority of actomyosin structures are known to undergo constriction to achieve complete closure, such as during cytokinesis, wound healing and dorsal closure. Specific actomyosin arrangements also provide scaffolding or stabilising force. The actomyosin association with the adherence junctions at the apical boundary of epithelia serves to stabilise the contact site and helps to recruit the junctional components (Lecuit et al., 2011; Schwayer et al., 2016; Zenker et al., 2018). In all these instances the actomyosin complex is organised in a ring-like form on a 2D-plane. Here, we showed that a 3-D membrane-actomyosin assembly could generate lateral constricting force orthogonal to the direction of intrusive force to clasp the spermatid heads together. This finding demonstrates a novel cell adhesion strategy, which is unprecedented. Further investigation is required to identify the physical basis of such an assembly and its functioning.

450 **Materials and Methods:**

451 *Drosophila* stocks and culture

452 All *Drosophila* stocks and crosses were maintained in standard cornmeal media at 25 °C. Male progeny
453 of *UAS-RNAi* crosses was collected and kept at 28 °C for 4 days, to achieve optimum Gal4 expression.
454 All the stocks have been listed in Table S1. All experiments involving transgenic *Drosophila* lines were
455 approved by the Institute Bio-Safety Committee, DBT, Govt. of India.

456 Whole-mount immunostaining

457 Testes were dissected in 1x PBS and fixed for 30 mins in 4% paraformaldehyde (PFA), followed by 3
458 washes of 10 mins each, with 0.3% PTX (0.3% Triton X 100 in 1 x PBS). Immunostaining samples were
459 then incubated in blocking buffer (2 mg/ ml Bovine Serum Albumin (BSA) in 0.3% PTX) for 30 mins,
460 followed by overnight incubation in the primary antibody. Samples were then washed and incubated
461 with Alexa-conjugated secondary antibodies (Invitrogen) for 2 hours, followed by incubation in 0.001%
462 Hoechst 33342 (Sigma-Aldrich), and 10 µM FITC Phalloidin/ Atto 647 Phalloidin (Sigma-Aldrich) for 30
463 min. Samples were then washed and mounted with a drop of Vectorshield™ mounting medium on a
464 glass slide. The primary antibodies used were anti-Fas III (1:100, DSHB), anti-Rho 1 (1:100, DSHB), anti-
465 Dia (1:2500, courtesy Prof. S Wasserman, UCSD) and anti-pMLC (1:25, Cell Signalling Technologies).

466 STED (Stimulated Emission Depletion)

467 For STED imaging, *ProtB-dsRed* testes were processed as described above and stained with Atto647-
468 Phalloidin. The samples were mounted on glycerol, and #1.5 coverslips were used. Depletion for both
469 fluorophores was done using a 775 nm laser. Time gating of 0.6<tg>6.6 was applied. Images were
470 acquired in 2D STED mode.

471 *Ex vivo* time-lapse imaging of testis

472 Live imaging was performed as described previously [9]. Images were acquired using either an Olympus
473 FV3000 confocal laser scanning microscope with 60x, 1.42 NA oil objective, or Olympus FV1000
474 confocal laser scanning microscope with 60x, 1.35 NA oil objective. Rockout (Calbiochem) was used at
475 a concentration of 200 µM. For FRAP, 1.4 μm^2 area in the basket was bleached to 60% level using high
476 intensity 488 nm laser for 2 seconds with 2 µs/pixel scan speed, and the recovery profile was recorded
477 at 5.5-second/frame rate. The data were analysed using ImageJ® and Origin™.

478

479

480 Laser ablation

481 Laser ablation was performed using the Spectra-Physics Mai Tai Ti-Sapphire laser system on Zeiss 710
482 microscope. For ablation, 408.2 mW of 800 nm laser was focussed in 0.75 μm^2 (10x10 pixels) area for
483 five iterations with a pixel dwell time of 12.6 µs/pixel.

484 Image Analysis and Quantification

485 All images were analysed on ImageJ/Fiji® (ImageJ.net/Fiji). We used the Cell Counter™ Plugin
486 for the NB and IC estimation and the FibrilTool Plugin (Boudaoud et al., 2014), which measures the
487 orientation and anisotropy of fibrillary structures, to assess the parallel organisation of spermatid
488 heads in each NB. A value of 1 indicates purely anisotropic (perfectly ordered or parallel), and 0
489 indicates disordered assembly. For FRAP, the intensities in the SUM projection was calculated from
490 the FRAP ROI, as well as an arbitrary background ROI. The data was normalised and fitted to a single
491 exponential using the Levenberg-Marquardt iteration algorithm in Origin™ 2019, based on which
492 maximum recovery was calculated. The basket volume was estimated using Imaris™ (Bitplane AG). A
493 volume filter of 100 voxels was applied, to eliminate stray F-actin puncta in the given ROI.

494 Statistical analyses (One-way ANOVA, Mann-Whitney Test) were carried out using Origin™ 2019.
495 Fisher's exact test was performed using the Graphpad online calculator. For box and dot plots, 'n'
496 values are indicated by the number of dots. For Fisher's exact test, 'n' values are indicated near the
497 pie chart or on the stacked bar graph.

498 Transmission Electron Microscopy

499 TEM samples were prepared as per the previous description (Dubey et al., 2019).

500

501 **Acknowledgements:**

502 We thank Richa Ricky, Benny Shilo, Steven Wasserman, Andrea Brand, John Belote, Vimlesh Kumar,
503 Thomas Lecuit, and Eyal Schejter for generous sharing of reagents. We acknowledge the BDSC, VDRC,
504 DSHB, and NCBS Fly Facility, India for providing fly stocks and antibodies. We also thank Lalit Borde for
505 help with TEM, and Hina Mohammed for assistance with the Synd mutant experiment.

506

507 **Authors' contributions:**

508 TK and PD performed the experiments. TK and KR wrote the manuscript. SS provided the TEM data.

Funding:

TK, PD and KR were supported by the intramural grant of Dept. of Atomic Energy (DAE), Government of India, to TIFR. The study was supported by the DAE, TIFR grant 12-R&D-TFR-5.10-100; Department of Atomic Energy, Government of India.

Disclosure statement:

The authors have no competing interests.

References:

Abagnale, G., Steger, M., Nguyen, V.H., Hersch, N., Sechi, A., Joussen, S., Denecke, B., Merkel, R., Hoffmann, B., Dreser, A., Schnakenberg, U., Gillner, A., Wagner, W., 2015. Surface topography enhances differentiation of mesenchymal stem cells towards osteogenic and adipogenic lineages. Biomaterials 61, 316-326.

Abreu-Blanco, M.T., Verboon, J.M., Parkhurst, S.M., 2014. Coordination of Rho family GTPase activities to orchestrate cytoskeleton responses during cell wound repair. Curr Biol 24, 144-155.

Amano, M., Nakayama, M., Kaibuchi, K., 2010. Rho-kinase/ROCK: A key regulator of the cytoskeleton and cell polarity. Cytoskeleton (Hoboken) 67, 545-554.

Aspenstrom, P., 2014. BAR domain proteins regulate Rho GTPase signaling. Small GTPases 5(2), 7.

Aspenstrom, P., Richnau, N., Johansson, A.S., 2006. The diaphanous-related formin DAAM1 collaborates with the Rho GTPases RhoA and Cdc42, CIP4 and Src in regulating cell morphogenesis and actin dynamics. Exp Cell Res 312, 2180-2194.

Boudaoud, A., Burian, A., Borowska-Wykret, D., Uyttewaal, M., Wrzalik, R., Kwiatkowska, D., Hamant, O., 2014. FibrilTool, an ImageJ plug-in to quantify fibrillar structures in raw microscopy images. Nat Protoc 9, 457-463.

Breitsprecher, D., Goode, B.L., 2013. Formins at a glance. J Cell Sci 126, 1-7.

Cundell, M.J., Price, C., 2014. The budding yeast amphiphysin complex is required for contractile actin ring (CAR) assembly and post-contraction GEF-independent accumulation of Rho1-GTP. PLoS One 9, e97663.

de Kreuk, B.J., Nethe, M., Fernandez-Borja, M., Anthony, E.C., Hensbergen, P.J., Deelder, A.M., Plomann, M., Hordijk, P.L., 2011. The F-BAR domain protein PACSIN2 associates with Rac1 and regulates cell spreading and migration. J Cell Sci 124, 2375-2388.

Desai, B.S., Shirolikar, S., Ray, K., 2009. F-actin-based extensions of the head cyst cell adhere to the maturing spermatids to maintain them in a tight bundle and prevent their premature release in Drosophila testis. BMC Biol 7, 19.

552 Dubey, P., Kapoor, T., Gupta, S., Shirolikar, S., Ray, K., 2019. Atypical septate junctions maintain the
553 somatic enclosure around maturing spermatids and prevent premature sperm release in Drosophila
554 testis. Biol Open 8.
555
556 Dubey, P., Shirolikar, S., Ray, K., 2016. Localised, Reactive F-Actin Dynamics Prevents Abnormal
557 Somatic Cell Penetration by Mature Spermatids. Dev Cell 38, 507-521.
558
559 Franke, J.D., Montague, R.A., Kiehart, D.P., 2010. Nonmuscle myosin II is required for cell proliferation,
560 cell sheet adhesion and wing hair morphology during wing morphogenesis. Dev Biol 345, 117-132.
561
562 Fricke, R., Gohl, C., Dharmalingam, E., Grevelhorster, A., Zahedi, B., Harden, N., Kessels, M., Qualmann,
563 B., Bogdan, S., 2009. Drosophila Cip4/Toca-1 integrates membrane trafficking and actin dynamics
564 through WASP and SCAR/WAVE. Curr Biol 19, 1429-1437.
565
566 Ghosh-Roy, A., Desai, B.S., Ray, K., 2005. Dynein light chain 1 regulates dynamin-mediated F-actin
567 assembly during sperm individualisation in Drosophila. Mol Biol Cell 16, 3107-3116.
568
569 Goh, W.I., Lim, K.B., Sudhaharan, T., Sem, K.P., Bu, W., Chou, A.M., Ahmed, S., 2012. mDia1 and WAVE2
570 proteins interact directly with IRSp53 in filopodia and are involved in filopodium formation. J Biol
571 Chem 287, 4702-4714.
572
573 Guttman, J.A., Takai, Y., Vogl, A.W., 2004. Evidence that tubulobulbar complexes in the seminiferous
574 epithelium are involved with internalisation of adhesion junctions. Biol Reprod 71, 548-559.
575
576 Hammer, J.A., Wang, J.C., Saeed, M., Pedrosa, A.T., 2019. Origin, Organization, Dynamics, and Function
577 of Actin and Actomyosin Networks at the T Cell Immunological Synapse. Annual Review of Immunology
578 37, 201-224.
579
580 Hinrichsen, L., Meyerholz, A., Groos, S., Ungewickell, E.J., 2006. Bending a membrane: how clathrin
581 affects budding. Proc Natl Acad Sci U S A 103, 8715-8720.
582
583 Kirchhausen, T., Owen, D., Harrison, S.C., 2014. Molecular structure, function, and dynamics of
584 clathrin-mediated membrane traffic. Cold Spring Harb Perspect Biol 6, a016725.
585
586 Kirchner, J., Gross, S., Bennett, D., Alphey, L., 2007. The nonmuscle myosin phosphatase PP1beta
587 (flapwing) negatively regulates Jun N-terminal kinase in wing imaginal discs of Drosophila. Genetics
588 175, 1741-1749.
589
590 Kuhn, S., Geyer, M., 2014. Formins as effector proteins of Rho GTPases. Small GTPases 5, e29513.
591 Lecuit, T., Lenne, P.F., Munro, E., 2011. Force generation, transmission, and integration during cell and
592 tissue morphogenesis. Annu Rev Cell Dev Biol 27, 157-184.
593
594 Liu, X., Billington, N., Shu, S., Yu, S.H., Piszczek, G., Sellers, J.R., Korn, E.D., 2017. Effect of ATP and
595 regulatory light-chain phosphorylation on the polymerisation of mammalian nonmuscle myosin II.
596 Proc Natl Acad Sci U S A 114, E6516-E6525.
597
598 Lou, H.Y., Zhao, W., Li, X., Duan, L., Powers, A., Akamatsu, M., Santoro, F., McGuire, A.F., Cui, Y., Drubin,
599 D.G., Cui, B., 2019. Membrane curvature underlies actin reorganisation in response to nanoscale
600 surface topography. Proc Natl Acad Sci U S A 116, 23143-23151.
601

602 Madasu, Y., Yang, C., Boczkowska, M., Bethoney, K.A., Zwolak, A., Rebowski, G., Svitkina, T.,
603 Dominguez, R., 2015. PICK1 is implicated in organelle motility in an Arp2/3 complex-independent
604 manner. Mol Biol Cell 26, 1308-1322.
605
606 Mizuno, T., Tsutsui, K., Nishida, Y., 2002. Drosophila myosin phosphatase and its role in dorsal closure.
607 Development 129, 1215-1223.
608
609 Murugesan, S., Hong, J., Yi, J., Li, D., Beach, J.R., Shao, L., Meinhardt, J., Madison, G., Wu, X., Betzig, E.,
610 Hammer, J.A., 2016. Formin-generated actomyosin arcs propel T cell receptor microcluster movement
611 at the immune synapse. Journal of Cell Biology 215, 383-399.
612
613 Nakamura, M., Verboon, J.M., Parkhurst, S.M., 2017. Prepatterning by RhoGEFs governs Rho GTPase
614 spatiotemporal dynamics during wound repair. J Cell Biol 216, 3959-3969.
615
616 Noguchi, T., Miller, K.G., 2003. A role for actin dynamics in individualisation during spermatogenesis
617 in Drosophila melanogaster. Development 130, 1805-1816.
618
619 Pontes, B., Ayala, Y., Fonseca, A.C., Romao, L.F., Amaral, R.F., Salgado, L.T., Lima, F.R., Farina, M.,
620 Viana, N.B., Moura-Neto, V., Nussenzveig, H.M., 2013. Membrane elastic properties and cell function.
621 PLoS One 8, e67708.
622
623 Rocca, D.L., Martin, S., Jenkins, E.L., Hanley, J.G., 2008. Inhibition of Arp2/3-mediated actin
624 polymerisation by PICK1 regulates neuronal morphology and AMPA receptor endocytosis. Nat Cell Biol
625 10, 259-271.
626
627 Schwayer, C., Sikora, M., Slovakova, J., Kardos, R., Heisenberg, C.P., 2016. Actin Rings of Power. Dev
628 Cell 37, 493-506.
629
630 Sherlekar, A., Rikhy, R., 2016. Syndapin promotes pseudocleavage furrow formation by actin
631 organisation in the syncytial Drosophila embryo. Mol Biol Cell 27, 2064-2079.
632
633 Takeda, T., Robinson, I.M., Savoian, M.M., Griffiths, J.R., Whetton, A.D., McMahon, H.T., Glover, D.M.,
634 2013. Drosophila F-BAR protein Syndapin contributes to coupling the plasma membrane and
635 contractile ring in cytokinesis. Open Biol 3, 130081.
636
637 Tokuyasu, K.T., Peacock, W.J., Hardy, R.W., 1972a. Dynamics of spermiogenesis in Drosophila
638 melanogaster. I. Individualisation process. Z Zellforsch Mikrosk Anat 124, 479-506.
639
640 Tokuyasu, K.T., Peacock, W.J., Hardy, R.W., 1972b. Dynamics of spermiogenesis in Drosophila
641 melanogaster. II. Coiling process. Z Zellforsch Mikrosk Anat 127, 492-525.
642
643 Viswanathan, P., Ondeck, M.G., Chirasatitsin, S., Ngamkham, K., Reilly, G.C., Engler, A.J., Battaglia, G.,
644 2015. 3D surface topology guides stem cell adhesion and differentiation. Biomaterials 52, 140-147.
645
646 Wiegand, T., Fratini, M., Frey, F., Yserentant, K., Liu, Y., Weber, E., Galior, K., Ohmes, J., Braun, F.,
647 Herten, D.-P., Boulant, S., Schwarz, U.S., Salaita, K., Cavalcanti-Adam, E.A., Spatz, J.P., 2020. Forces
648 during cellular uptake of viruses and nanoparticles at the ventral side. Nature Communications 11, 32.
649
650 Yamada, H., Padilla-Parra, S., Park, S.J., Itoh, T., Chaineau, M., Monaldi, I., Cremona, O., Benfenati, F.,
651 De Camilli, P., Coppey-Moisan, M., Tramier, M., Galli, T., Takei, K., 2009. Dynamic interaction of
652 amphiphysin with N-WASP regulates actin assembly. J Biol Chem 284, 34244-34256.

Yan, S., Lv, Z., Winterhoff, M., Wenzl, C., Zobel, T., Faix, J., Bogdan, S., Grosshans, J., 2013. The F-BAR protein Cip4/Toca-1 antagonises the formin Diaphanous in membrane stabilisation and compartmentalisation. J Cell Sci 126, 1796-1805.

Yang, S., Saif, M.T., 2007. Force response and actin remodeling (agglomeration) in fibroblasts due to lateral indentation. Acta Biomater 3, 77-87.

Yarrow, J.C., Totsukawa, G., Charras, G.T., Mitchison, T.J., 2005. Screening for cell migration inhibitors via automated microscopy reveals a Rho-kinase inhibitor. Chem Biol 12, 385-395.

Yoshida, S., Bartolini, S., Pellman, D., 2009. Mechanisms for concentrating Rho1 during cytokinesis. Genes Dev 23, 810-823.

Zenker, J., White, M.D., Gasnier, M., Alvarez, Y.D., Lim, H.Y.G., Bissiere, S., Biro, M., Plachta, N., 2018. Expanding Actin Rings Zipper the Mouse Embryo for Blastocyst Formation. Cell 173, 776-791 e717.

Zhao, H., Michelot, A., Koskela, E.V., Tkach, V., Stamou, D., Drubin, D.G., Lappalainen, P., 2013. Membrane-sculpting BAR domains generate stable lipid microdomains. Cell Rep 4, 1213-1223.

Zhao, W., Hanson, L., Lou, H.Y., Akamatsu, M., Chowdary, P.D., Santoro, F., Marks, J.R., Grassart, A., Drubin, D.G., Cui, Y., Cui, B., 2017. Nanoscale manipulation of membrane curvature for probing endocytosis in live cells. Nat Nanotechnol 12, 750-756.

676 **Main Figures and legends:**

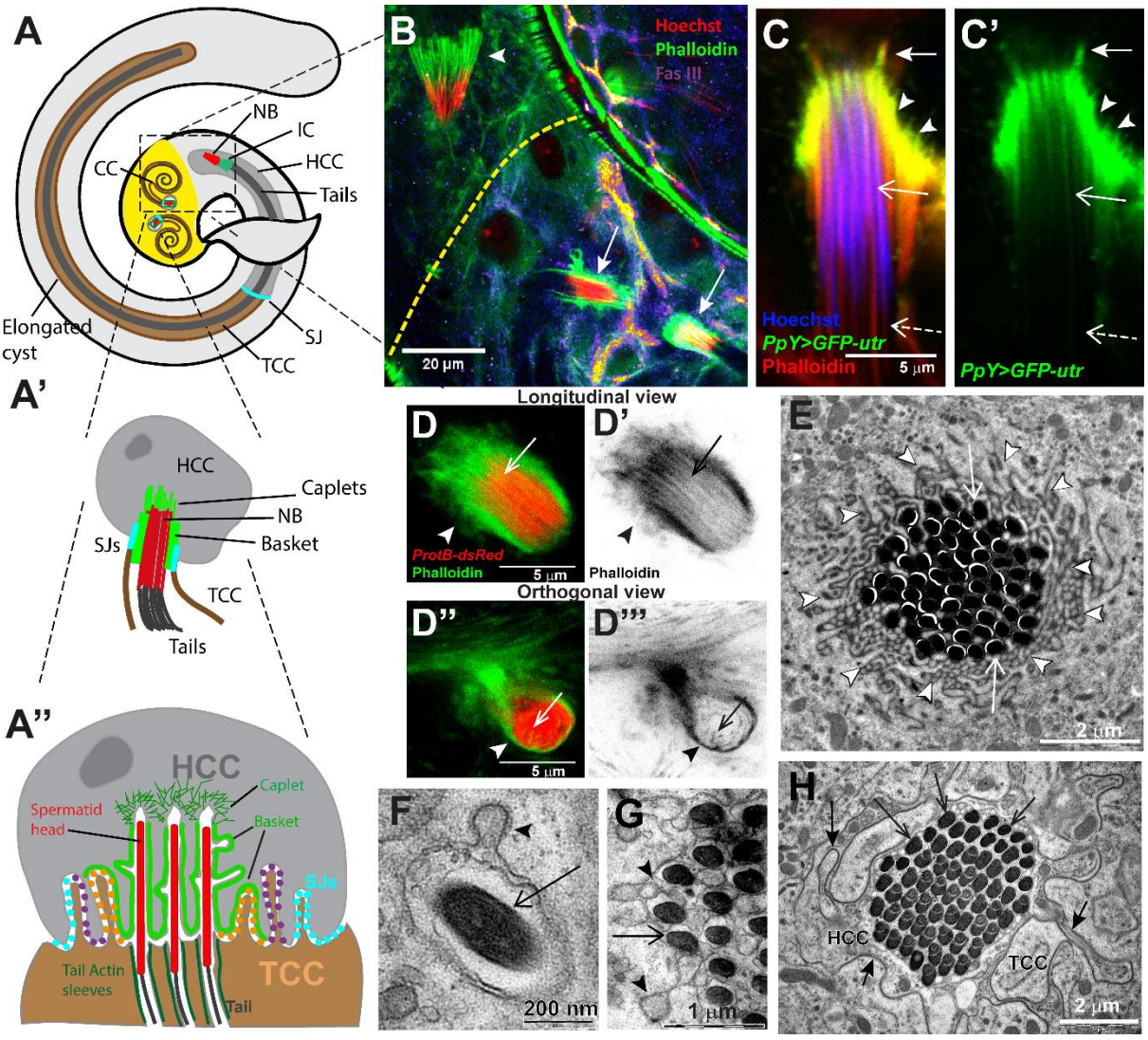

677

678

679 **Figure 1- Tubular, actin-rich membrane covers individual spermatid heads within a cyst during the**
680 **final stages of sperm maturation in *Drosophila* testis.**

681 **A-A'')** Schematic of *Drosophila* testis. Sixty-four spermatids synchronously develop within the cyst
682 enclosure. After individualisation, the elongated spermatid tails (dark grey) coil up inside the cyst and
683 move to the TE region (yellow zone) at the base of the testis. The NBs (red) of coiled spermatids are
684 covered by an actin cap (green), consisting of basket and caplet domains. **A'** and **A"** depicts the
685 expanded views of the arrangement inside the HCC. As depicted in **A",** each spermatid head is
686 enclosed with an actin-rich membrane sleeve. The HCC-TCC interface is highly folded, and marked by
687 the SJs.

688 **B)** Confocal image of a wild-type testis, stained with Hoechst dye (red), marking the spermatid heads,
689 and Phalloidin (green) marking F-actin. Actin-caps form around the spermatid head bundles (NB, red)
690 (arrows) once the cyst is inside the TE region. The yellow dashed line marks the boundary of TE region
691 marked by the Fas-III immunostaining (Fire LUT). Arrowhead indicates the spermatid head bundle of
692 an early individualising cyst, with associated IC at the caudal end of the NB outside the TE region.

693 **C-C')** *PpY>GFP-utr* (green) expression in cyst cells, stained with Hoechst (blue) and Phalloidin (red).
694 The caplets (arrow) and the basket domains (arrowheads), as well as a part the actin sleeves (open
695 arrows), are marked by the GFP-Utr.

696 **D-D''')** STED microscopy images of NB (red) and associated actin cap (green) in *ProtB-dsRed* expressing
697 testis, stained with Phalloidin. The longitudinal view (D-D') shows that the actin structure is present in
698 between the packing of individual sperm heads (arrows). Orthogonal section (D''-D''') through the NB
699 also depicts the presence of actin in the region between individual sperm heads (arrows). Arrowheads
700 mark the basket actin surrounding the entire bundle.

701 **E-H)** TEM images of transverse sections of NBs from wild-type testes depict spermatid heads (open
702 arrows, E) surrounded by extensively folded and tubular membrane (arrowheads, E) near the tips of
703 the spermatid heads, which are buried relatively deeper inside the HCC. Such tubular membrane was
704 not visible at the level of the HCC-TCC junction (arrows, F). High magnification images of individual
705 spermatid heads inside the HCC (G) shows two layers of plasma membrane surrounding each
706 spermatid head. The outer layer, likely to be contributed by the HCC, have tubulobulbar extensions
707 (arrowheads, H).

708

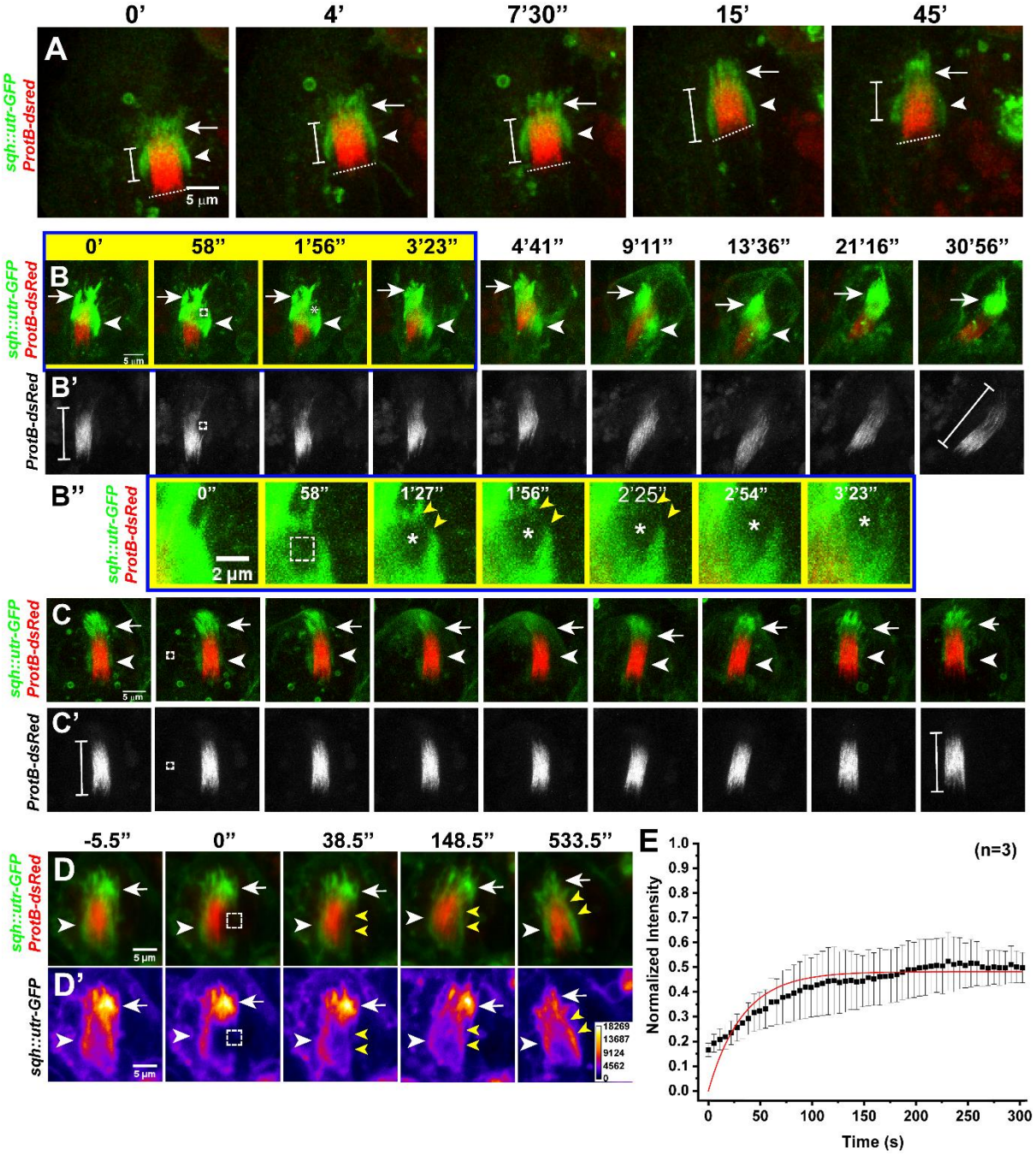

Figure 2- Basket domain maintains the spermatid heads in a bundle.

A) Time-lapse images of *sqh::utr-GFP; ProtB-dsRed* expressing testis, depicting the actin cap (green) around the NB (red). Arrow indicates the caplet; the arrowheads indicate the basket domain, and the dashed line denotes the caudal end of the NB. Note that the length of the basket, indicated by the scale bar, oscillates along the long axis.

B-C) Time-lapse images after part ablation (dashed outline) of the basket domain (B-B''), and a control spot in the HCC cytoplasm (C-C'), of *sqh::utr-GFP; ProtB-dsRed* testes, using 800 nm laser. Arrows mark

718 the caplets; the arrowheads mark basket and asterisks mark the centre of the ablated ROI. Closed lines
719 indicate the length of the NB, before ablations, and at 30'56". (B") High magnification images of 0-
720 3'23" frames of B, showing the expanding edges of the ablated region (yellow arrowheads).

721 **D)** Fluorescence recovery after photobleaching (FRAP) of *sqh::utr-GFP* in the basket domain. The
722 intensity profile is depicted in a false colour heat map (FIRE, D'). The dashed outline marks the
723 photobleached ROI; yellow arrowheads mark the photobleached zone during recovery; the
724 arrowheads mark the basket domain, and the arrows mark the caplets.

725 **E)** The FRAP recovery profile (mean ± S.D.) fitted with the Levenberg-Marquardt iteration algorithm.

726

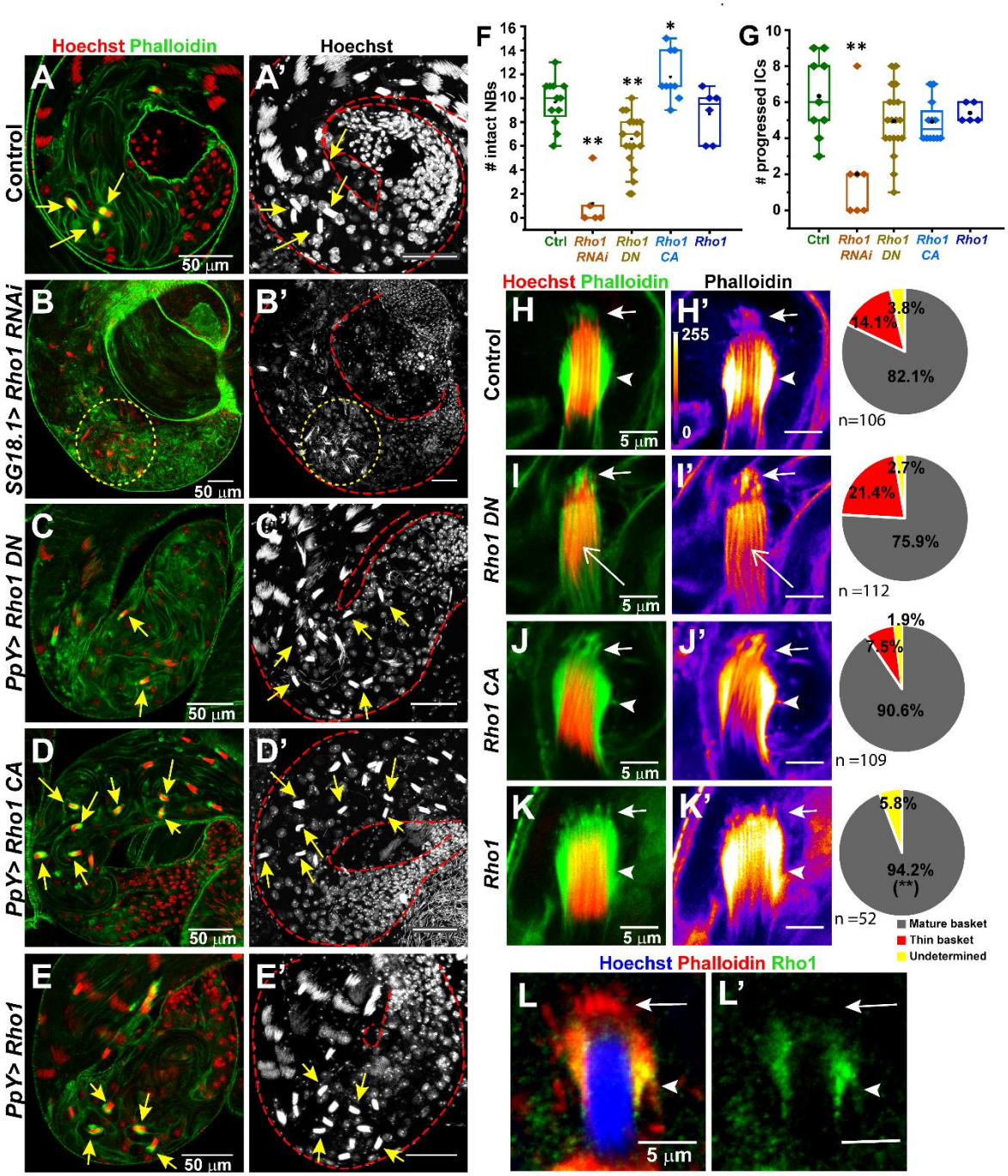

Figure 3- Rho 1 perturbation in the cyst cells affects the stability of the basket domain and NB.

A-E) Confocal sections of testis base from the Control (A-A'), *SG18.1>Rho1* RNAi (B-B'), *PpY>Rho1N19DN* (C-C'), *PpY>Rho1V14CA* (D-D') and *PpY>Rho1* (E-E') backgrounds, stained with the Hoechst (red/ white) and Phalloidin (green). Arrows indicate intact NBs associated with baskets. A'-E' represent maximum intensity projections of Hoechst channel, depicting all the NBs in the testes.

F-G) Box plots depict the number of intact NBs (F) and the progressed ICs (G) upon Rho 1 perturbations in the cyst cells. The pairwise significance with respect to the control value was estimated using One-

735 way Anova® and Mann-Whitney U tests, respectively, and the p-values- * <0.05, ** <0.01, *** < 0.001
736 are indicated on each box.

737 **H-K**) High magnification images of an NB associated with the actin cap from the control (G-G'), *Rho*
738 *1DN* (I-I'), *Rho 1CA* (J-J'), and *Rho 1* (**J-J'**) expressing testes, stained with Hoechst (red) and Phalloidin
739 (green/ FIRE). Arrows, arrowheads and open arrows indicate caplets, basket, and actin sleeves,
740 respectively. Pie charts indicate relative proportions of different basket morphologies classified as
741 mature (as shown in Fig S1F), thin (as shown in S1G), and undetermined. The pairwise significance
742 with respect to the control value was estimated using Fisher's Exact test, and the p-values- * <0.05,
743 ** <0.01, *** < 0.001 are indicated on the pie chart.

744 **L-L)** NB and the associated basket domain stained with anti-Rho1 (green), Hoechst (blue), and
745 Phalloidin (red). Note that Rho1 is enriched at the basket domain (arrowhead), and not in the caplet
746 (arrow).

747

748

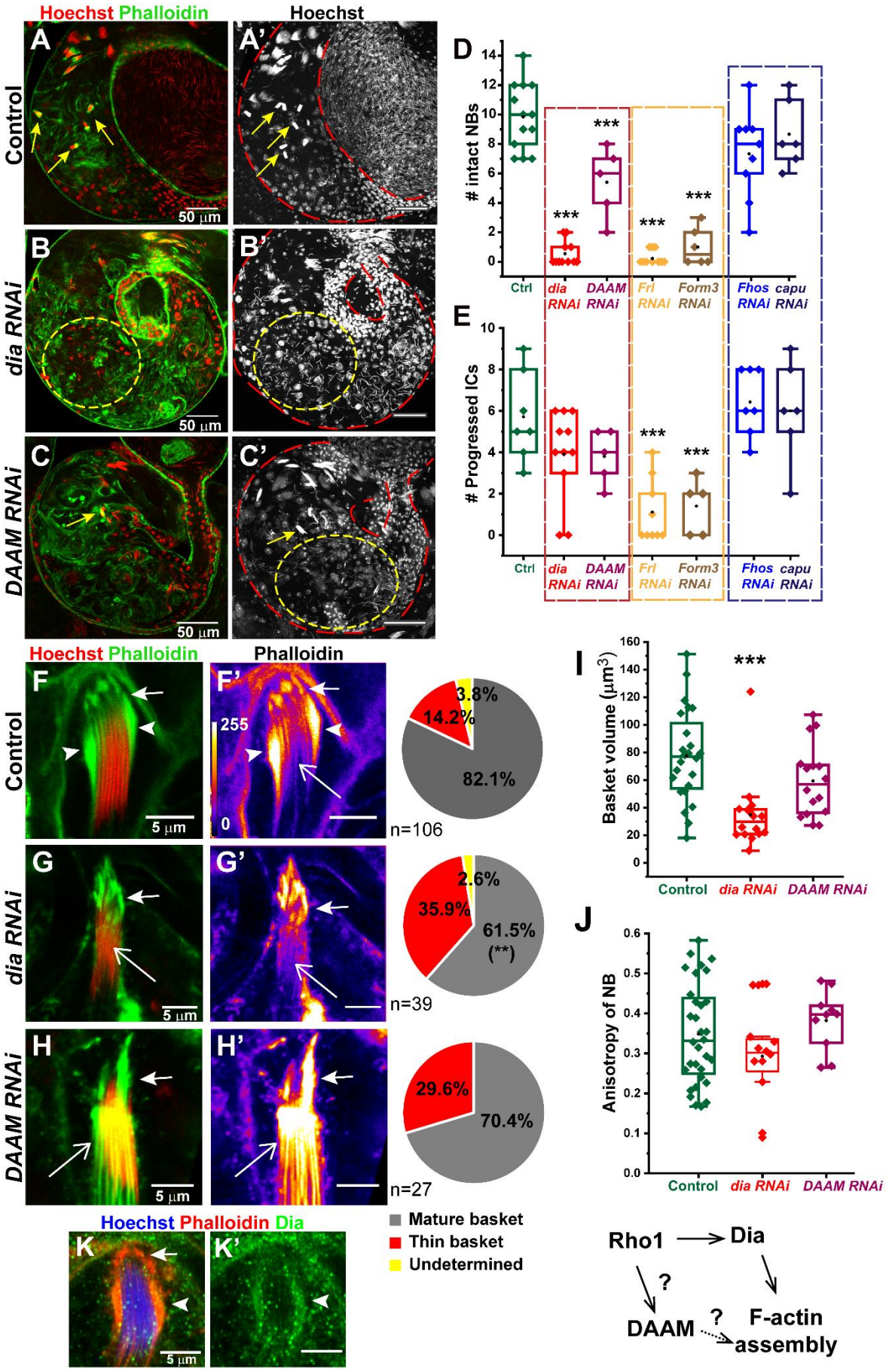
Hoechst Phalloidin
Hoechst
Control
dia RNAi
DAAM RNAi
A
A'
B
B'
C
C'
50 µm
D
intact NBs
Ctrl
dia RNAi
DAAM RNAi
Frl RNAi
Form3 RNAi
Fhos RNAi
capu RNAi
***
E
Progressed ICs
Hoechst Phalloidin
Phalloidin
F
F'
G
G'
H
H'
255
0
5 µm
3.8%
14.2%
82.1%
n=106
2.6%
35.9%
61.5%
(**)
n=39
29.6%
70.4%
n=27
Mature basket
Thin basket
Undetermined
I
Basket volume (µm³)
Control
dia RNAi
DAAM RNAi
J
Anisotropy of NB
Hoechst Phalloidin Dia
K
K'
Rho1
Dia
?
DAAM
F-actin assembly

749

750 **Figure 4- F-actin, nucleated by the formin, Diaphanous, constitutes the basket domain.**

751 **A-C)** TE region of *PpY>GFP* (Control, A-A'), *PpY> dia RNAi* (B-B') and *PpY> DAAM RNAi* (C-C') testes
752 stained with Hoechst (red/ white) and Phalloidin (green). A'-C' represent maximum intensity
753 projections, depicting all the NBs in the TE region.

754 **D-E)** Box plots depict the number of intact NBs (D) and the progressed ICs (E) on perturbation of six
755 different formins in the cyst cells. The pairwise significance with respect to the control value was
756 estimated using Mann-Whitney U tests, and the p-values- * <0.05, ** <0.01, *** < 0.001 are indicated
757 on each box.

758 **F-H)** High magnification images of NBs stained with Hoechst (red) and Phalloidin (green/FIRE), from
759 the control (F-F'), *dia* (G-G') and *DAAM* (H-H') RNAi testes. Pie charts indicate relative proportions of
760 different basket phenotypes. Arrows, arrowheads and open arrows indicate caplets, basket, and actin
761 sleeves, respectively. Significance was calculated using Fisher's exact test, and the p values - * <0.05,
762 ** <0.01, *** < 0.001 are indicated on the pie charts.

763 **I-J)** Box and dot plots depict the volume of the basket domain (I) and the organisation (Anisotropy) of
764 spermatid head alignment in the NBs (J) in Control, *dia* and *DAAM* RNAi backgrounds. The pairwise
765 significance of difference with respect to the control values was estimated using Mann-Whitney U
766 tests and One-way Anova®, respectively, and the p-values- * <0.05, ** <0.01, *** < 0.001 are indicated
767 on each box.

768 **K)** NB and the associated basket domain stained with anti-Dia (green), Hoechst dye (blue), and
769 Phalloidin (red). Note that Diaphanous is enriched at the basket domain (arrowheads), and not in the
770 caplet (arrow).

771

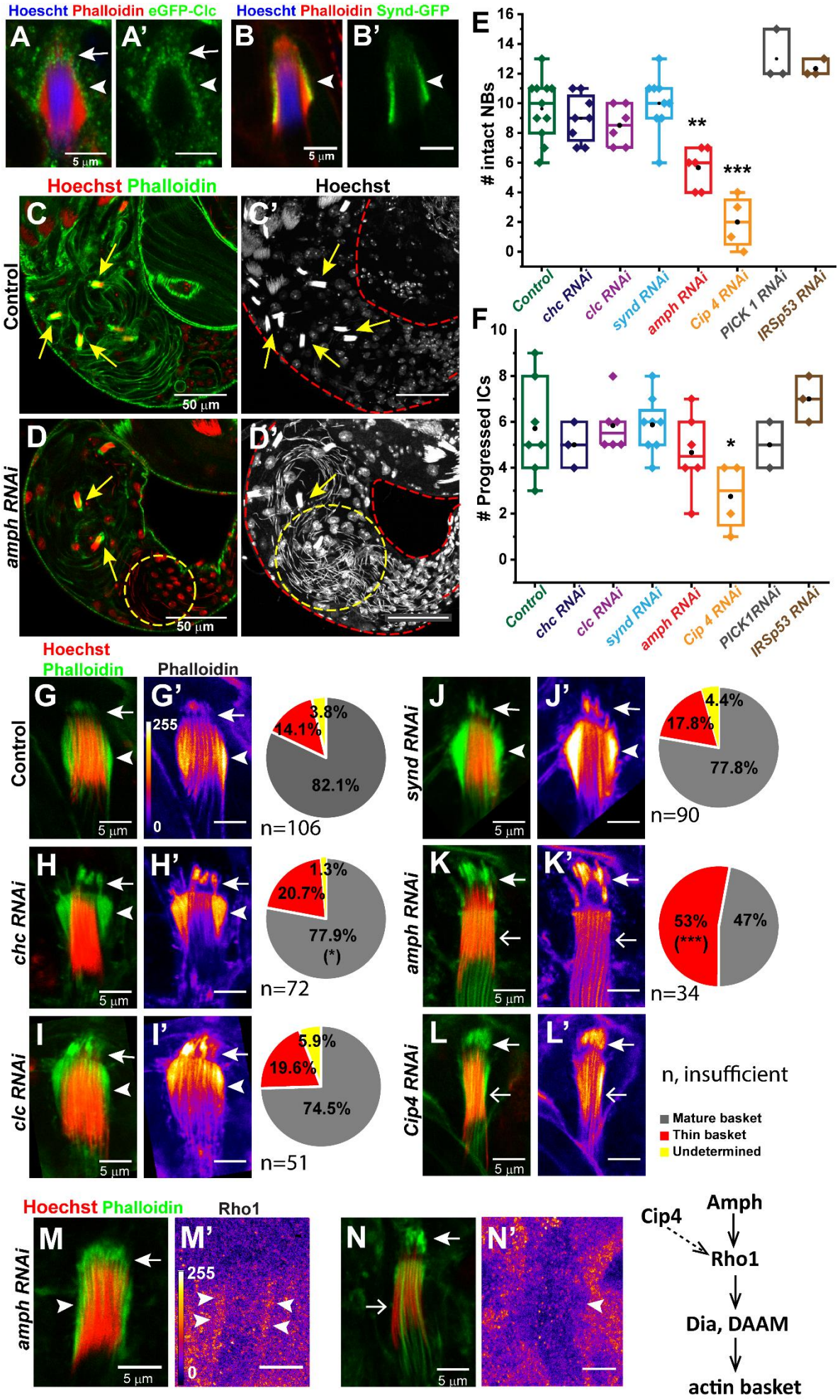
Hoescht Phalloidin eGFP-Clc
Hoescht Phalloidin Synd-GFP
A
A'
B
B'
5 µm
Hoechst Phalloidin
Hoechst
C
C'
D
D'
Control
amph RNAi
50 µm
E
intact NBs
**
***
Control
chc RNAi
clc RNAi
synd RNAi
amph RNAi
Cip 4 RNAi
PICK 1 RNAi
IRSp53 RNAi
F
Progressed ICs
*
PICK1RNAi
Hoechst
Phalloidin
Phalloidin
G
G'
255
0
3.8%
14.1%
82.1%
n=106
J
J'
synd RNAi
4.4%
17.8%
77.8%
n=90
H
H'
chc RNAi
1.3%
20.7%
77.9%
(*)
n=72
K
K'
amph RNAi
53%
(***)
47%
n=34
I
I'
clc RNAi
5.9%
19.6%
74.5%
n=51
L
L'
Cip4 RNAi
n, insufficient
Mature basket
Thin basket
Undetermined
Hoechst Phalloidin
Rho1
M
M'
N
N'
Cip4
Amph
Rho1
Dia, DAAM
actin basket

773 **Figure 5- The F-BAR proteins, Amphiphysin and Cip4, are required to assemble the basket domain.**

774 **A-B)** Clathrin-Light-Chain (*PpY>e-GFP clc)* (A-A'), and Syndapin (*PpY> synd-GFP*) (B-B') localisations
775 around and in the basket domain (arrowheads).

776 **C-D)** Confocal images of TE of Control (C-C') and *amph RNAi* (D-D') testes, stained with Hoechst (red/
777 white) and Phalloidin (green). C', D' represent maximum intensity projections of the Hoechst channel,
778 depicting all the NBs in the testes. Yellow arrows mark intact testes, and yellow dashed circle marks
779 disrupted NBs.

780 **E-F)** Box and dot plots depicting the number of intact NBs (E) and the progressed ICs (F) in the testes
781 expressing different RNAi constructs in the cyst cells. The pairwise significance of difference with
782 respect to the control value was estimated using Mann-Whitney U tests, and the p-values- * <0.05, **
783 <0.01, *** < 0.001 are indicated on each box.

784 **G-L)** The morphology of the caplet (arrows) and the basket (arrowheads) domains in different RNAi
785 backgrounds, stained with the Hoechst dye (red) and Phalloidin (green/ FIRE). F-actin levels are
786 depicted in a false colour heat map (FIRE) in the right panels, and the associated pie charts depict the
787 penetrance of the phenotypes in these backgrounds. Open arrows indicate actin sleeves around the
788 spermatid tails.

789 **M-N)** Rho1 localisation (FIRE, M', N') in the *amph RNAi* background, stained with the Hoechst dye (red)
790 and Phalloidin (green). Arrows indicate the caplets, arrowheads indicate the basket, and the open
791 arrow indicates the actin sleeve, respectively.

792

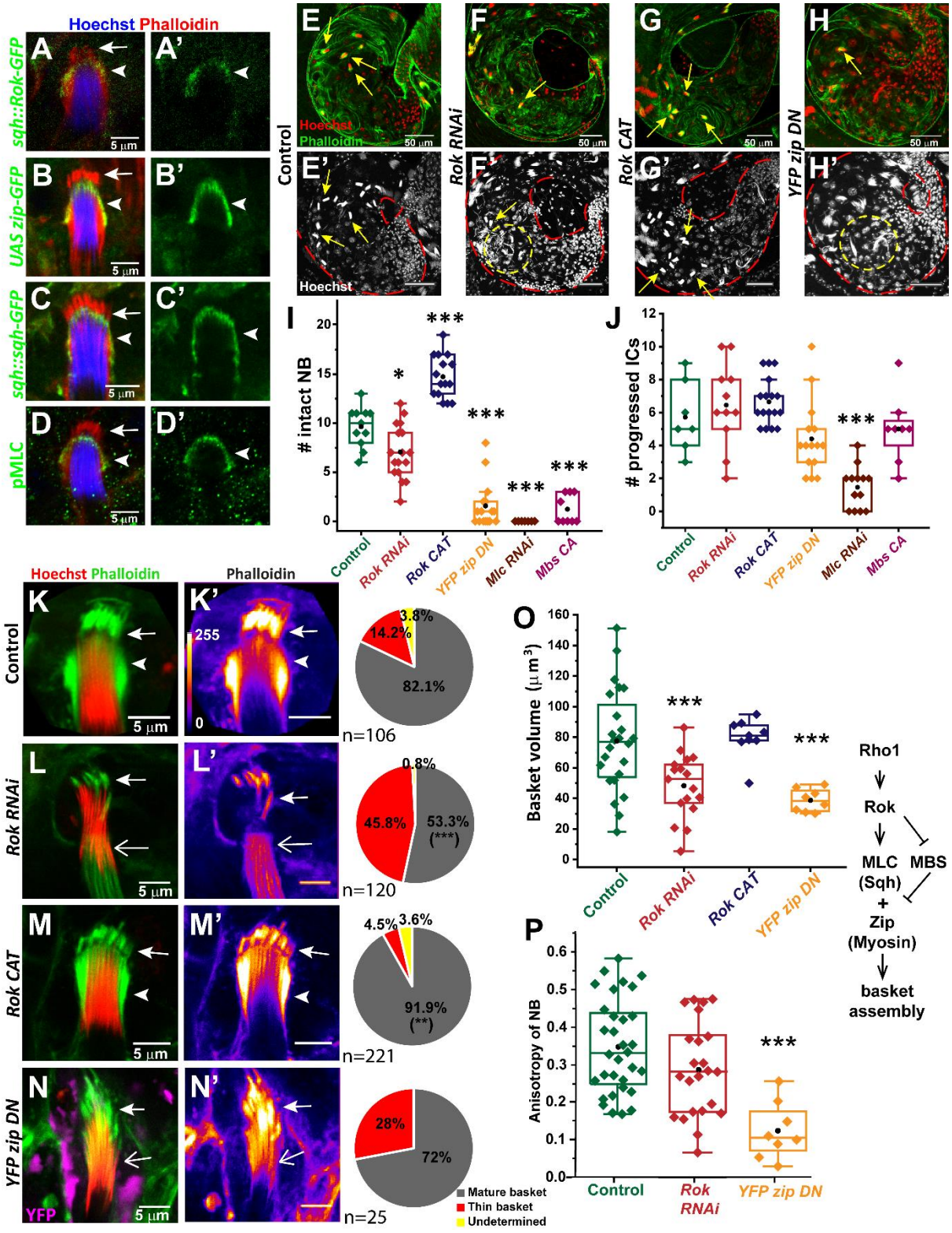

Figure 6- Rok and nonmuscle myosin-II (Zipper) function is essential for the basket assembly.

A-D) NB from testis expressing (green) *Sqh*::*Rok-GFP* (A-A'), *PpY>zip-GFP* (B-B'), *sqh::sqh-GFP* (C-C'), and stained with anti-pMLC (D-D'), respectively, along with Hoechst dye (blue) and Phalloidin (red).

797 Note that the localisation pattern is restricted to the basket (arrowheads) domain, and is absent from
798 the caplets (arrows).

799 **E-H)** TE regions of Control (E-E'), *PpY>Rok RNAi* (F-F'), *PpY> Rok-CAT* (G-G'), and *PpY>YFP-zip DN* (H-H')
800 testes, stained with Hoechst (red/ white), and Phalloidin (green).

801 **I-J)** Box plots depict the number of intact NBs (I) and the number of progressed ICs (J) in different
802 genetic backgrounds. The pairwise significance of difference with respect to the control value was
803 estimated using Mann-Whitney U tests, and the p-values- * <0.05, ** <0.01, *** < 0.001 are indicated
804 on each box.

805 **K-N)** High magnification images depict the morphology of the actin cap in Control (K-K'), *Rok RNAi* (L-
806 L'), *Rok CAT* (M-M') and *YFP-zip DN* (N-N') backgrounds, stained with Hoechst (red) and Phalloidin
807 (green/FIRE). Arrows indicate the caplet, arrowheads indicate basket, and the open arrow indicates
808 the actin sleeves around the spermatids. The F-actin levels are shown in false colour (K'-N') intensity
809 heat map according to the LUT on K'. Pie charts depict the frequency of different basket phenotypes.
810 The significance was calculated using the Fisher's exact test, and the p-values- * <0.05, ** <0.01, ***
811 < 0.001 are indicated on each box.

812 **O-P)** Box plots depict the volume of the basket domain (O) and the organisation (Anisotropy) of the
813 spermatid head alignment in NBs (P) in the Control, *Rok RNAi* and *YFP-zip DN* testes, respectively.
814 Significance was calculated using One-way Anova®, and the p-values- * <0.05, ** <0.01, *** < 0.001
815 are indicated on each box.

816

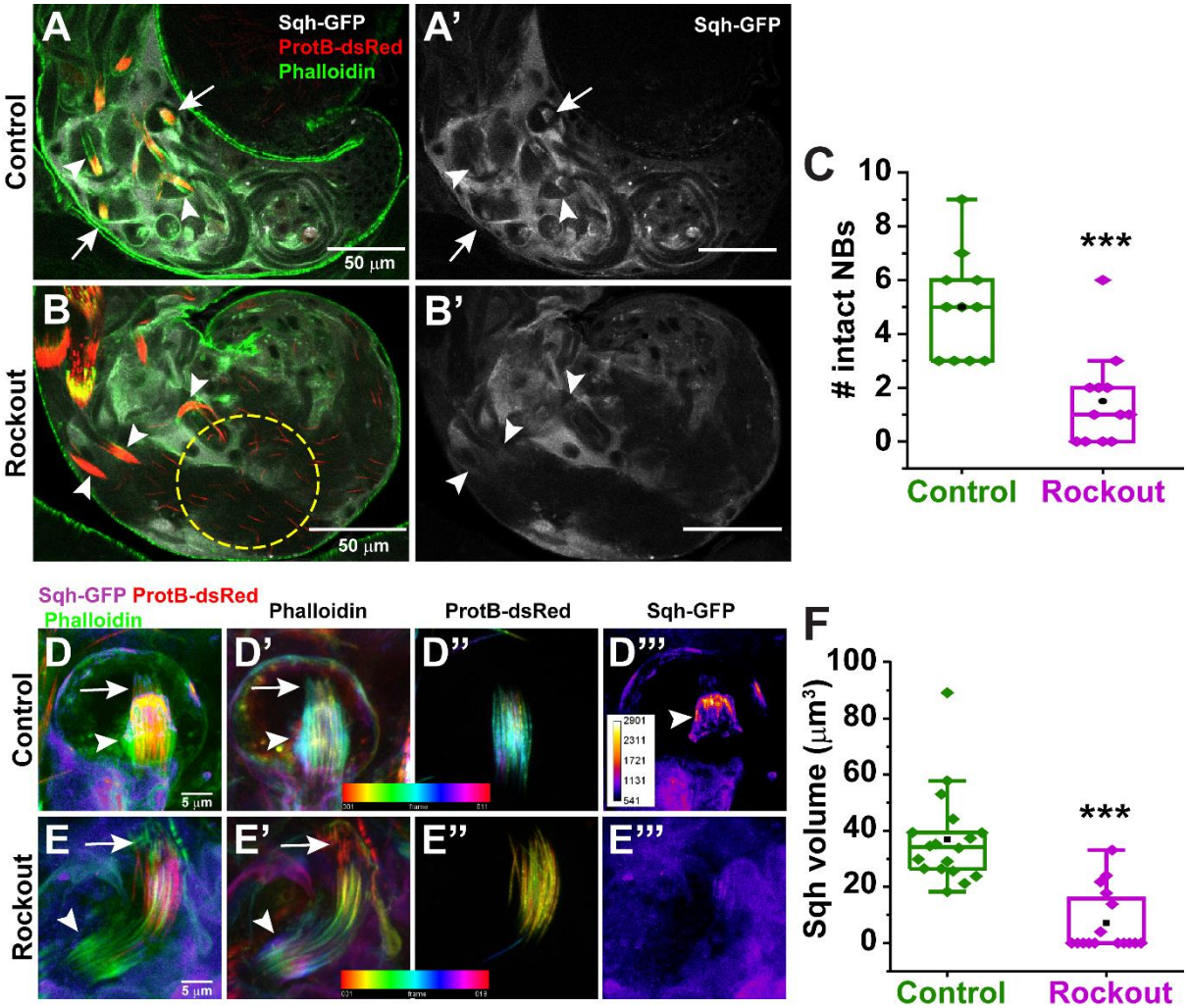
A
Sqh-GFP
ProtB-dsRed
Phalloidin
A'
Sqh-GFP
Control
50 µm
B
B'
Rockout
50 µm
C
intact NBs
10
8
6
4
2
0
***
Control
Rockout
Sqh-GFP ProtB-dsRed
Phalloidin
Phalloidin
ProtB-dsRed
Sqh-GFP
D
D'
D''
D'''
Control
5 µm
E
E'
E''
E'''
Rockout
5 µm
F
Sqh volume (µm³)
100
80
60
40
20
0
***
Control
Rockout

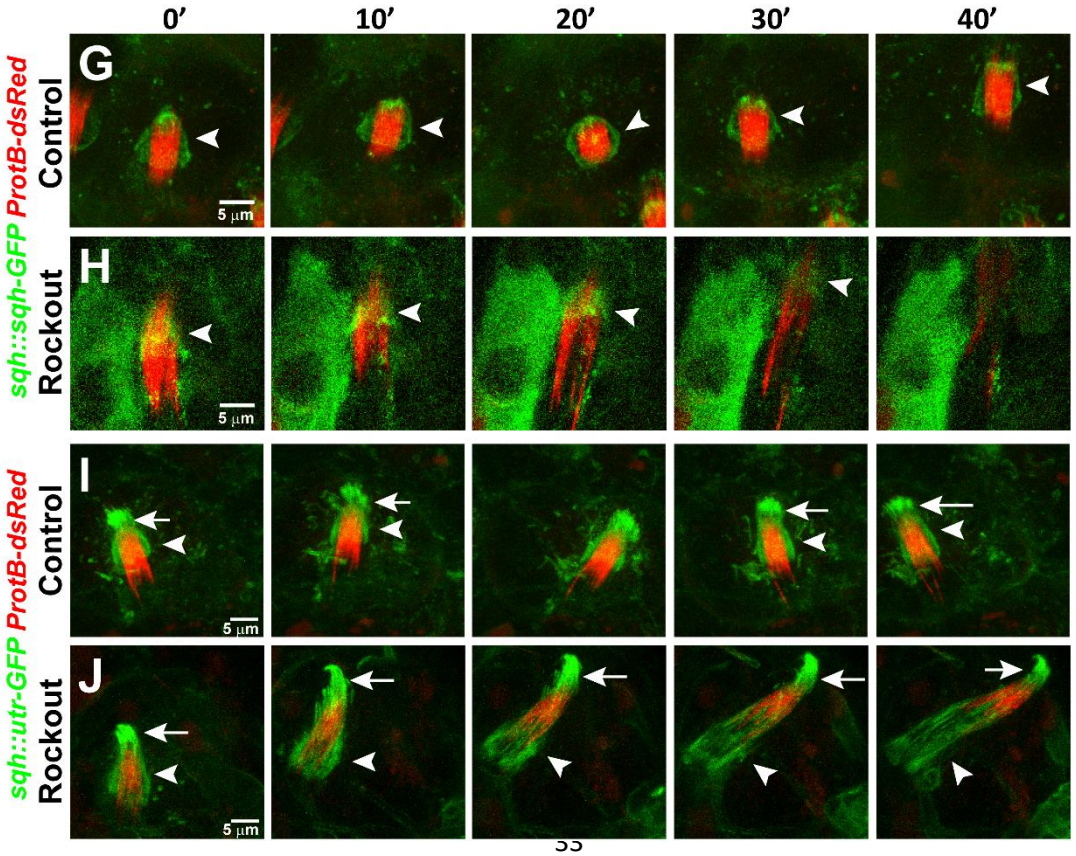
0'
10'
20'
30'
40'
G
Control
5 µm
H
Rockout
5 µm
sqh::sqh-GFP ProtB-dsRed
I
Control
5 µm
J
Rockout
5 µm
sqh::utr-GFP ProtB-dsRed

817

818 **Figure 7- NM2 activity at the basket is essential for compaction of the spermatid heads into a tight**
819 **bundle.**

820 **A-B)** Confocal images from *sqh::sqh-GFP* (white) and *ProtB-dsRed* (red) expressing testes, treated with
821 2% DMSO (Control, A-A') and 200 µM Rockout (B-B'), for one hour and stained with Phalloidin (green).
822 Arrows mark intact bundles, arrowheads mark bundles which have been perturbed by DMSO/ Rockout
823 treatment. Yellow dashed circle marks the disrupted sperm heads.

824 **C**) The number of intact NBs in control and Rockout treated testes. Pair-wise significance of difference
825 was estimated using Mann-Whitney U test, and the p-values- * <0.05, ** <0.01, *** < 0.001 are
826 indicated on the box.

827 **D-E)** High magnification images of NBs from Control (D-D''') and Rockout treated testes (E-E'''). D, E
828 represents the merged images, depicting Sqh-GFP (FIRE), ProtB-dsRed (red) and Phalloidin (green).
829 Arrows mark caplet, and arrowhead marks basket. D-D'' and E-E'' represent depth coded Z-stack for
830 Phalloidin (D', E') and ProtB-dsRed (D'', E'') in Control (D'-D'') and Rockout treated (E'-E'') testes,
831 respectively. The colour code is according to the scale depicted in the images. The Fire LUT (E''')
832 represents the intensity heat map.

833 **F)** Basket volume marked by Sqh-GFP in Control and Rockout treatment testes. Significance was
834 calculated using Mann-Whitney U test, and the p-values- * <0.05, ** <0.01, *** < 0.001 are indicated
835 on the box.

836 **G-J)** Time-lapse images of testes expressing *sqh::sqh-GFP* and *ProtB-dsRed* (G, H), and *sqh::utr-GFP*
837 and *ProtB-dsRed* (I, J), respectively, after the DMSO (Control) and Rockout treatments. The arrows
838 indicate caplet and the arrowheads indicate the basket domains.

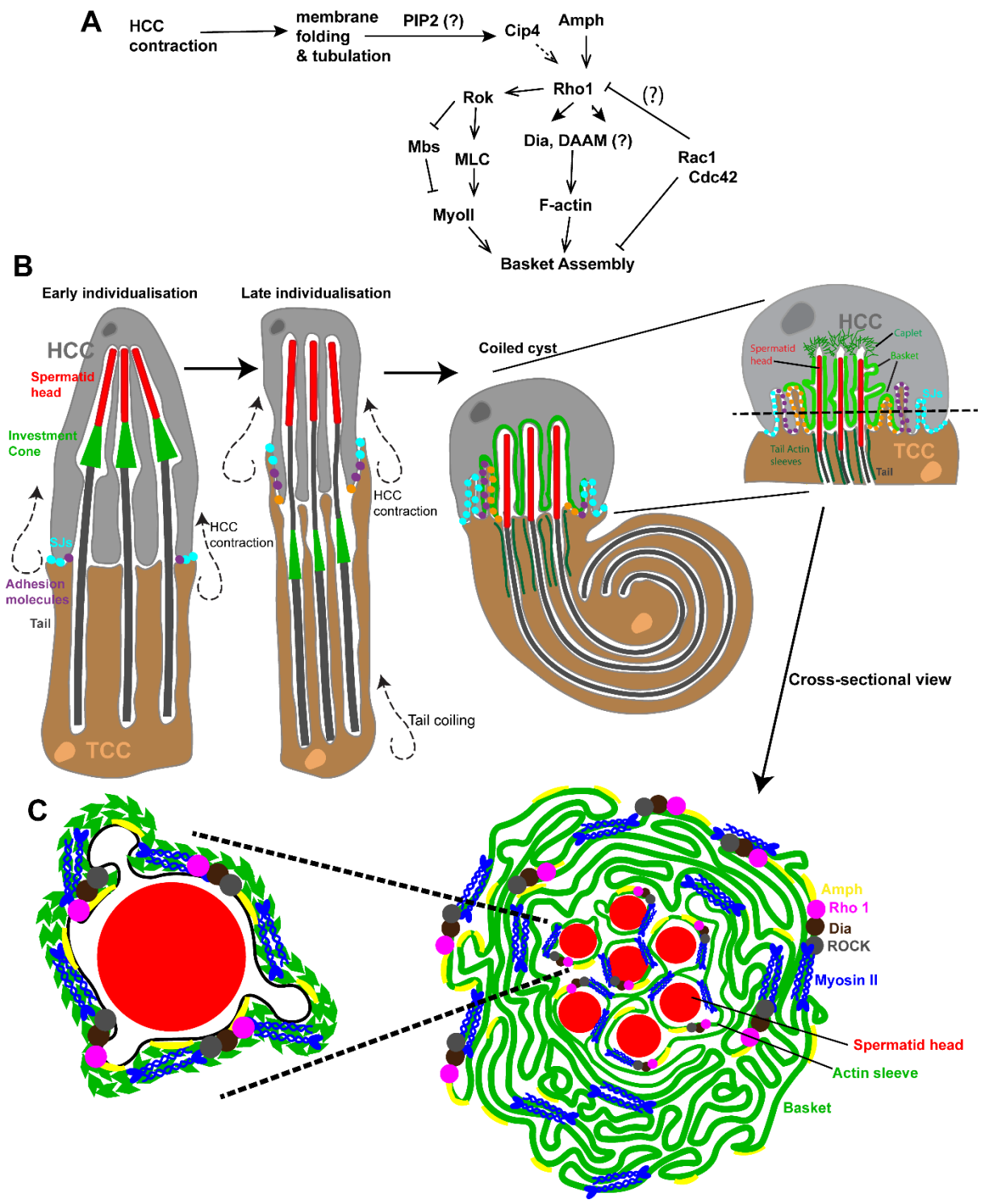

Figure 8- Assembly of the contractile actomyosin scaffold around mature spermatid heads butting into the somatic head cyst cell.

Flow chart and schematic depict how remodelling of the membrane during individualisation to coiling transition of the cyst, can potentially recruit Amph, which may intern recruit Rho 1. Rho 1 forms the basket and maintains NB arrangement, via the activation of the formins, Dia and DAAM, and the Rho kinase Rok, which in turn activates NM-2.